Synchronous Ensembles of Hippocampal CA1 Pyramidal Neurons During Novel Exploration

En-Li Chen[1,2], Tsai-Wen Chen[1,2], Eric R. Schreiter[3], Bei-Jung Lin[1,2*]

[1]Institute of Neuroscience, National Yang Ming Chiao Tung University, Taipei, Taiwan
[2]Brain Research Center, National Yang Ming Chiao Tung University, Taipei, Taiwan
[3]Janelia Research Campus, Howard Hughes Medical Institute, Ashburn, VA 20147, USA.
*Corresponding author: beijunglin@nycu.edu.tw

Abstract

Synchronous neuronal ensembles play a pivotal role in the consolidation of long-term memory in the hippocampus. However, their organization during the acquisition of spatial memory remains less clear. In this study, we used neuronal population voltage imaging to investigate the synchronization patterns of CA1 pyramidal neuronal ensembles during the exploration of a new environment, a critical phase for spatial memory acquisition. We found synchronous ensembles comprising approximately 40% of CA1 pyramidal neurons, firing simultaneously in brief windows (~25ms) during immobility and locomotion in novel exploration. Notably, these synchronous ensembles were not associated with contralateral ripple oscillations but were instead phase-locked to theta waves recorded in the contralateral CA1 region. Moreover, the subthreshold membrane potentials of neurons exhibited coherent intracellular theta oscillations with a depolarizing peak at the moment of synchrony. Among newly formed place cells, pairs with more robust synchronization during locomotion displayed more distinct place-specific activities. These findings underscore the role of synchronous ensembles in coordinating place cells of different place fields.

Introduction

The establishment of long-term memory involves the initial acquisition and subsequent consolidation of memory traces, processes intricately connected to the modification of synaptic transmission[1,2]. Synchronous ensembles, characterized by the simultaneous firing of multiple neurons over tens of milliseconds (referred to as population synchrony), play a pivotal role in influencing synaptic plasticity[3-5]. The hippocampus, a crucial region for long-term memory formation[6,7], has been a focal point of synchronous ensemble studies. Within the hippocampus, synchronous ensembles are hypothesized to play roles in reactivating and consolidating labile memory traces[8]. However, their organization during memory acquisition remains less understood.

In the hippocampus, synchronous ensembles among CA1 pyramidal cells (CA1PCs) are predominantly observed during sharp-wave ripples, the brain waves associated with memory consolidation[8-13]. During these events, 10-18% of CA1PCs generate spikes, particularly during offline consummatory behavioral states or sleep[14,15]. These synchronous ensembles are biased toward experience-dependent reactivation, consolidating labile memory traces[16,17]. Furthermore, synchronous ensembles firing action potentials in short windows of 10-30 milliseconds enhance information processing[6] and discriminate distinct behavioral contingencies[18]. Although synchronous ensembles of CA1PCs during offline memory consolidation are well-characterized, their organization during online acquisition of spatial memory, such as when animals enter a new environment and new place cells form, remains unclear.

Previous studies have identified correlated activities among place cells during theta oscillation, where 1-3% of place cells' spikes co-activate in a forward order matching animals' trajectory in the theta cycles when animals' locations overlap in the place fields of these cells[19-21]. Because these place cells fire at distinct theta phases in the same cycle, this coordinated firing operates on the timescale of theta periods (~125ms)[22,23]. Population synchrony on shorter timescales (10-30 ms) is

52 speculated to be reduced by the presence of theta oscillations[22].

53

54 The subthreshold membrane voltage (subVm), influenced by synaptic inputs and intrinsic
55 conductances, directly triggers spiking activity[24,25]. Additionally, properties of subVm support the
56 organization of neuronal representation[26]. Although correlated membrane potentials have been
57 proposed to underlie the synchrony of neuronal ensembles[27,28], multicellular recordings of subVms
58 have not yet provided direct experimental evidence. Given the intricate interaction among subVm,
59 spiking, and place cell formation, it is crucial to investigate the temporal relationships of sub- and
60 suprathreshold neuronal activities among CA1PCs during novel exploration.

61

62 In this study, we used voltage imaging to investigate the temporal dynamics of sub- and
63 suprathreshold neuronal activities in CA1PCs during novel exploration. Additionally, we implanted
64 electrodes in the contralateral CA1 region to monitor theta and ripple oscillations, which are known
65 to co-occur across hemispheres[29-31]. We found synchronous ensembles involving approximately 40%
66 of CA1PCs exhibited transient population synchrony and correlated subthreshold membrane
67 potentials when mice ran and stopped in a new maze. Surprisingly, these synchronous ensembles
68 occurred outside of contralateral ripples and were phase-locked to intracellular theta oscillations as
69 well as extracellular theta oscillations recorded from the contralateral CA1 region. Notably, cell pairs
70 with stronger synchronous activities established more distinct place fields that overlapped less. In
71 essence, synchronous ensembles facilitated temporal association among place cells representing
72 diverse features of spatial memory. This plastic network, driven by synchronous ensembles, may
73 contribute to the stabilization of place cells, establishing place fields that effectively tile the
74 environment.

75

76 **Results**

77 To investigate the temporal relationships between neuronal activities during novel exploration, we

simultaneously recorded many neurons as animals explored a new environment for the first time. To achieve this, we employed voltage imaging in conjunction with an air-lifted plastic track that allowed mice to explore an environment while remaining head-fixed under a microscope (Figure 1A). To ensure a genuinely novel experience, all pre-training and habituation were performed in a separate room distinct from the one where the imaging experiments were conducted. On the day of imaging, the mice were introduced to the recording room for the first time and initially confined to a specific corner of the track (Figure 1A top view). Subsequently, as the imaging session commenced, the confinement was lifted, granting mice the freedom to explore the track while imaging was conducted.

In novel exploration, mice moved at a speed of 8.3±0.9 cm/s during locomotion (speed>3 cm/s) and spent 53±7% and 36±6% of their time in locomotion and immobility (speed<1 cm/s), respectively (n=5 mice). Meanwhile, they completed 10±2.5 laps during the 180-s imaging periods (n=5 mice).

For voltage imaging, we expressed the voltage indicator Voltron2[32] in CA1 pyramidal cells (CA1PCs) that were born on embryonic day (E) 14.5, allowing us to measure both suprathreshold and subthreshold membrane potentials from multiple CA1PCs (14±4 cells imaged per field of view (mean±s.d.) and, in total, 71 cells imaged from 5 fields of view in 5 mice; Figure 1B, Supplementary Figure 1A, 1B). Simultaneously, we monitored the animals' positions and speed within the track while recording the local field potential (LFP) from the contralateral side of the hippocampus (Figure 1B, Figure 1-figure supplement 1). Consistent with previous studies, neurons labeled on E14.5 located more on the deep side of the pyramidal layer than those labeled on E17.5 ($t_{(601)}$=22.8, p<0.0001, Student's t-test; Supplementary Figure 1C, D)[33-37].

The mean firing rates of cells ranged from 2.3 to 4.3 Hz (25th-75th percentiles) with a median of 3.2 Hz (n=71 cells, Supplementary Figure 2A). Additionally, most CA1PCs exhibited elevated mean firing

rates during immobility relative to locomotion, and their firing rates showed a negative correlation with the animals' speed (Supplementary Figure 2B, 2C), consistent with previous research[38].

Synchronous ensembles among many CA1 pyramidal neurons

Figure 1C shows the fluorescence traces of all neurons in a session as an example. Instances of synchronous activity, where many neurons emitted spikes within a narrow time window, were frequently observed (Figure 1C). To investigate synchronous activity within the neuronal population, we selected a reference cell and counted the number of spikes across all other cells that were aligned with the spikes of the reference cell. This approach yielded a grand average cross-correlogram (CCG) capable of elucidating the timing of spikes from the reference cell relative to the combined spikes of the rest of the population. Notably, the grand average CCG exhibited heightened spike counts around zero lags, unlike flattened counts calculated from randomly selected cells of different sessions (Figure 1D and 1E). The full width at half maximum (FWHM) of the peak in the grand average CCG measured 23±14 ms (mean±s.d., n=71 cells from 5 sessions; Figure 1F), indicating the timescale of the population synchrony. Furthermore, pairwise CCGs of many cell pairs showed significant peaks compared to jittered data (percentage of significant pairs: 63% (median) n=497 pairs, Figure 1-figure supplement 2A and 2B). Among pairs with significant peaks, the absolute values of the peak lags ranged from 0.8 to 4.3 ms (25th-75th percentiles) with a median of 2.1 ms, and the FWHM of the peaks ranged from 20 to 46 ms (25th-75th percentiles) with a median of 30 ms (n=315 pairs, Figure 1-figure supplement 2C and 2D). These results highlight the synchronous spiking between neurons on the millisecond timescale.

To systematically reveal individual synchronous events, we counted the number of spikes from all simultaneously recorded neurons within sliding windows of 25 ms. To compare the summed spikes with controls, we randomly jittered the spike trains to perturb spike timings while maintaining spike rates. We identified moments of population synchrony when spike sums exceeded the average of

130 the jittered spike sums plus four standard deviations (Figure 1C). Using the same criterion for event
131 detection, we observed over a 7.8-fold increase in synchronous events in the original data
132 compared to jittered controls (mean event rate: 0.94±0.17 Hz for the original data, 0.12±0.01 Hz for
133 the jittered data, n=10 segments, p=0.002, W=55, Wilcoxon signed-rank test; Figure 1G). The
134 observed population synchrony was not attributable to spikes in complex bursts, as synchronous
135 event rates did not differ significantly with or without the inclusion of later spikes in bursts
136 (Supplementary Figure 3). Furthermore, we calculated the percentage of neurons participating in
137 these synchronous events to examine the synchronous ensemble sizes. The ensemble sizes ranged
138 from 32% to 53% (25th-75th percentiles) with a median of 42%, which were larger than the
139 synchronous ensemble sizes associated with ripples[14] (Figure 1H). These results demonstrate
140 synchronous ensembles of CA1PCs engaging many neurons.
141

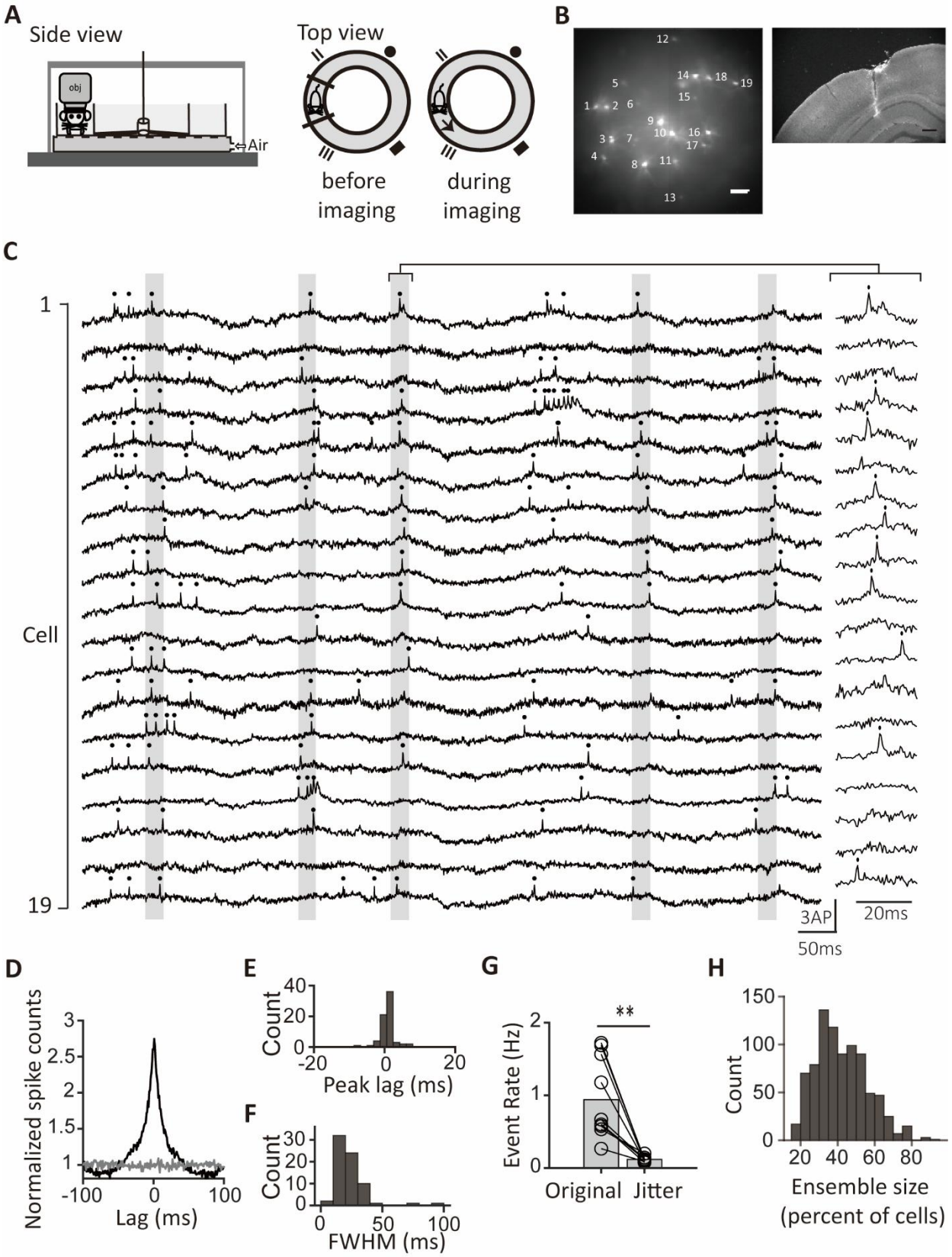

Figure 1. Population synchrony during novel exploration.

(A) Schematic of the behavioral setup for voltage imaging. Mice explored a novel one-way track

while fluorescence images were captured at the CA1 pyramidal layer. Left: side view; right: top view of the setup.

(B) Left: example time-averaged image of CA1 pyramidal cells expressing Voltron2-ST labeled with JF_{552}-HaloTag ligand. Scale bar, 100 μm. Right: a microphotograph of a brain slice with the contralateral LFP electrode track from the same mouse as the left. Scale bar, 300 μm.

(C) Fluorescence traces of cells in an example session with identified synchronous ensembles (labeled with gray vertical bars). Right: an example of magnified fluorescence traces within the bracket, pinpointing the occurrence of the identified synchronous ensemble. Spikes are indicated by dots on the top.

(D) The grand average cross-correlogram (CCG) averaged across all 71 cells. The gray line represents the mean grand average CCG between reference cells and randomly selected cells from different sessions.

(E) Distribution of the grand average CCG peak lags of all cells (n=71).

(F) Distribution of the full width at half maximum (FWHM) of the grand average CCGs (n=71 cells).

(G) Pairwise comparison of the event rates of population synchrony between original and jittered data. Bar heights indicate group means. **p<0.01

(**H**) Histogram of the ensemble sizes as percentages of cells participating in the synchronous ensembles.

Synchronous ensembles during locomotion and immobility of novel exploration

The hippocampus exhibits state-dependent activities when rodents are engaged in locomotion and immobility[38,39]. In novel exploration, CA1PCs showed synchronous spiking during locomotion and immobility (Figure 2A). To investigate whether these synchronous activities differed between these behavioral states, we compared grant average CCGs and synchronous ensembles under these conditions. During both immobility and locomotion, grant average CCGs showed prominent peaks

compared to jittered data (Figure 2B). Moreover, synchronous ensembles were rich in both immobility and locomotion periods (Figure 2A, 2B and 2D). Nevertheless, the FWHMs of grand average CCGs were broader in the immobility group compared to the locomotion group (Figure 2B and 2C). Synchronous events occurred more frequently during immobility compared to locomotion (Figure 2D). Additionally, ensemble sizes were significantly larger in the immobility group compared to the locomotion group (Figure 2E). Taken together, with differences in sizes and kinetics, there were synchronous ensembles during both immobility and locomotion periods of novel exploration.

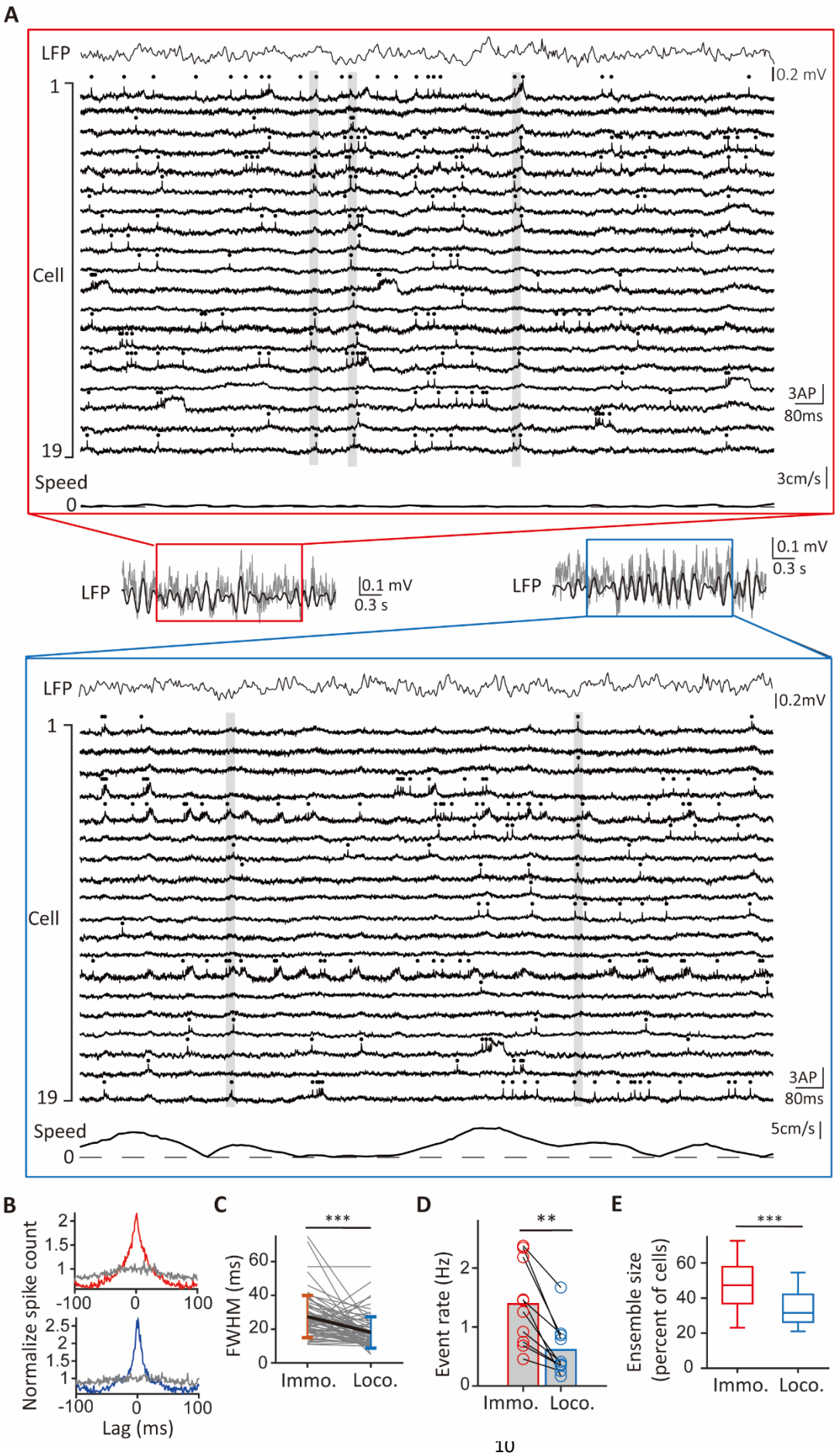
A
LFP
0.2 mV
1
Cell
19
3AP
80ms
Speed
0
3cm/s
LFP
0.1 mV
0.3 s
LFP
0.1 mV
0.3 s
LFP
0.2mV
1
Cell
19
3AP
80ms
Speed
0
5cm/s
B
Normalize spike count
Lag (ms)
C
FWHM (ms)
Immo.
Loco.
D
Event rate (Hz)
Immo.
Loco.
E
Ensemble size (percent of cells)
Immo.
Loco.

178

179 **Figure 2. Comparison of synchronous ensembles between immobility and locomotion.**

180 **(A)** Example traces of cells in a session with identified synchronous ensembles (gray vertical bars)
181 during periods of immobility (red rectangular frame) and locomotion (blue rectangular frame).
182 Spikes are indicated by dots at the top of individual traces. Top: the simultaneously recorded LFP
183 trace. Bottom: simultaneously recorded speed of the animal. Inset: the band-pass filtered LFP trace
184 at the theta frequency range (black line) overlaid on the raw LFP trace (gray line).

185 **(B)** The grand average cross-correlograms (CCGs) during immobility (red) and locomotion (blue)
186 averaged across all cells (n=71). The gray lines represent the mean grand average CCGs calculated
187 from jittered data.

188 **(C)** Pairwise comparison of peak widths (FWHM) in the grand average CCGs between immobility
189 (red) and locomotion (blue). Vertical bars represent means and standard deviations for both groups
190 (FWHM: 27±12 ms for immobility, 18±9 ms for locomotion, mean±s.d., $t_{(70)}$=5.45, p<0.001, paired t-
191 test, n=71 cells). ***p<0.001

192 **(D)** Pairwise comparison of event rates of population synchrony during immobility and locomotion.
193 Bar heights indicate group means (immobility: 1.4±0.7 Hz, locomotion: 0.6±0.5 Hz, mean±s.d., n=10
194 segments, W=55, p=0.002, Wilcoxon signed-rank test). **p<0.01

195 **(E)** Boxplot of ensemble sizes for synchronous ensembles occurring during immobility (red) and
196 locomotion (blue) (median ensemble size: 47% for immobility, n=446 events, 32% for locomotion,
197 n=313 events, $t_{(757)}$=13.54, p<0.001, Student's t-test). ***p<0.001

198

199

200 ## Synchronous ensembles occur outside ripple episodes

201 CA1PCs exhibit synchronous activities when the hippocampal network emits ripple waves[8,14]. To test
202 whether there is a co-occurrence of synchronous ensembles and contralateral ripples, we first
203 detected ripples from LFP recordings. Ripples were detected in three of the five recording sessions,
204 and all occurred during immobility (mean ripple rate: 0.04±0.02 Hz during immobility, 0 Hz during

205 locomotion). In the two recording sessions where we did not detect any ripples, we verified the
206 recording quality of the LFP signal by running multiple tests after the recording sessions. Ripples
207 were identified in the same animals during quality tests, indicating that the absence of ripples
208 during novel immobility in the recording session was not due to the deterioration of LFP recordings
209 (Figure 3-figure supplement 1).
210
211 To visualize both ripples and synchronous ensembles, we plotted voltage traces of neurons
212 alongside simultaneously recorded ripple oscillations. It was typical for synchronous ensembles to
213 occur far away from ripple episodes (Figure 3A). To delve into the relationship between neuronal
214 activities and ripples, we aligned traces of ripple power with population synchrony and ripples. In a
215 recording session where 64 synchronous ensembles and 12 ripples were detected during
216 immobility, the LFP power at ripple frequency (120-240 Hz) exhibited no discernable peaks within
217 any of the synchronous events (Figure 3B, left upper and middle panels). Nevertheless, the same
218 LFP power displayed substantial peaks during every ripple event (Figure 3B, right upper and middle
219 panels). A striking contrast between synchronous events and ripples was also evident when spiking
220 probabilities during these events were examined. During population synchrony, the mean spiking
221 probability averaged across all cells was high, while the spiking probability was almost zero during
222 ripple events (Figure 3B lower panel). In the three sessions where ripples were identified, we
223 calculated the percentages of ripple events coinciding with synchronous ensembles and vice versa.
224 Remarkably, there was no co-occurrence of ripples and synchronous ensembles (Figure 3C).
225 Furthermore, we quantified ripple-modulated spiking by calculating the ratio of the difference in
226 mean firing rates during in-ripple and out-ripple periods to the sum of the mean firing rates during
227 both periods. Indexes of most cells were negative, and a striking 85% of cells displayed ripple
228 modulation indexes of -1, indicating complete suppression of their spiking activities during ripples
229 (Figure 3D). Taken together, during novel exploration, synchronous ensembles involved many
230 neurons with millisecond-synchronized spikes and occurred outside the time frames of ripples.

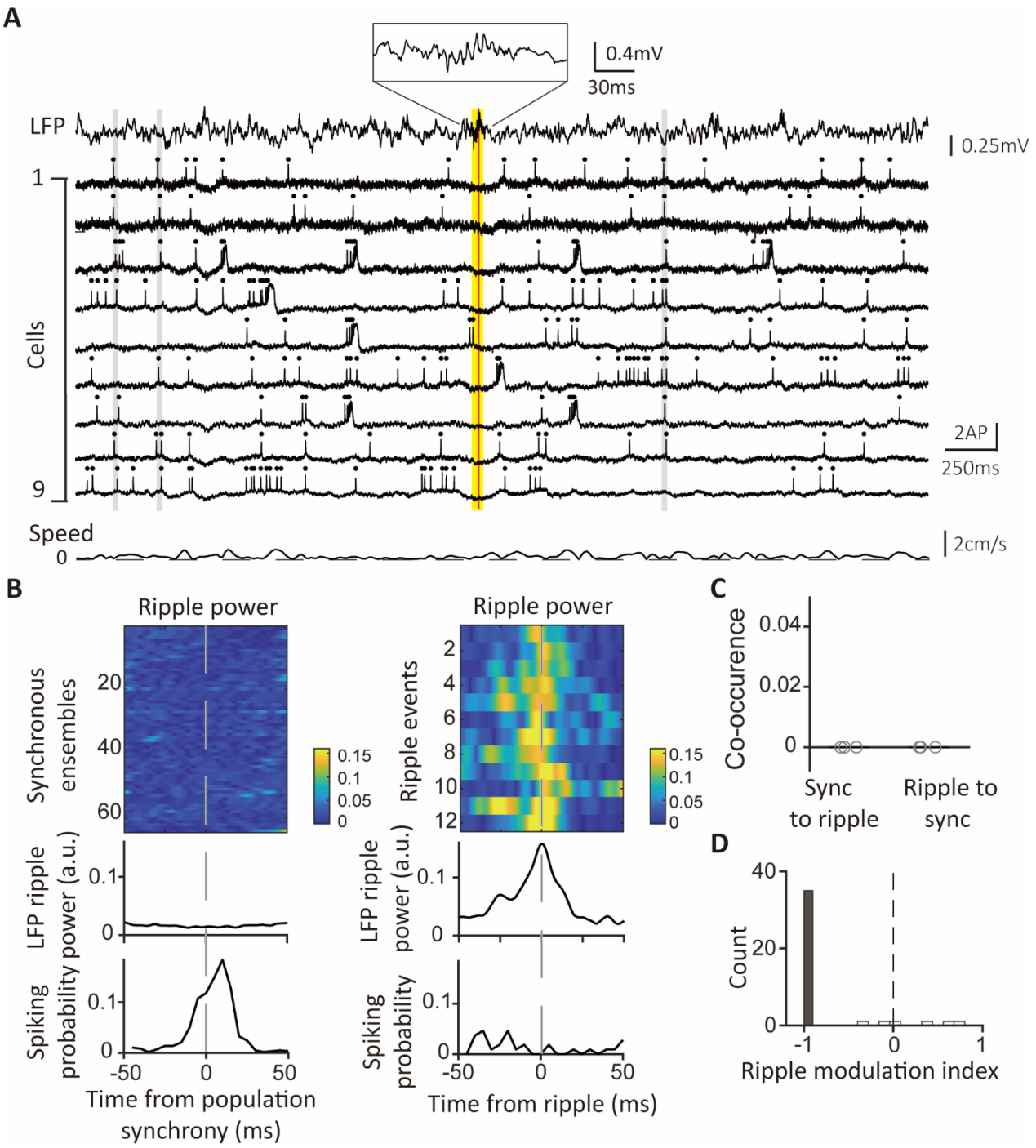

Figure 3. Synchronous ensembles occur outside ripple episodes.

(A) Example traces with ripples and synchronous ensembles. Top: simultaneously recorded LFP displaying an episode of ripple oscillation. A red vertical line indicates the timing of the peak ripple power in the LFP trace. A yellow vertical bar marks the duration of the ripple episode. Inset at the top: a magnified view of the ripple oscillation. Middle: fluorescence traces of 9 CA1PCs. Gray

238 vertical bars mark the timings of the synchronous ensembles on all traces. Bottom: animals' speed
239 recorded simultaneously with voltage imaging.
240 **(B)** LFP ripple power and spiking probability aligned to synchrony ensembles and ripple events.
241 Upper panel: color-coded LFP power at ripple frequency (120-240Hz) aligned to the timings of 64
242 synchronous ensembles (left) and 12 ripple events (right). Middle panel: Average LFP power of
243 ripple frequency aligned to the timings of the synchronous ensembles (left) and the ripple events
244 (right). Lower panel: Average spike counts of all cells aligned to the timings of the synchronous
245 ensembles (left) and ripple events (right).
246 **(C)** Percentages of co-occurrences between population synchrony and ripples. The co-occurrences
247 in the "sync to ripples" group represent the percentages of ripple episodes co-occurring with
248 synchronous ensembles in the same episodes. The co-occurrences in the "ripples to sync" group
249 indicate the percentages of synchronous ensembles co-occurring with ripple episodes. Each gray
250 circle represents an individual session.
251 **(D)** Distribution of the ripple modulation indexes (*n*=41 cells). Gray bar: modulation indexes with
252 significant p values (*n*=35 cells); white bars: modulation indexes without significance (*n*=6 cells).
253
254 It was puzzling that these CA1PCs exhibited robust spiking activities outside of ripples yet generated
255 few spikes during ripples. To further investigate neuronal activities during ripples, we established a
256 recording condition that allowed us to capture more ripple episodes. Specifically, we immobilized
257 mice in a tube to promote behaviors favoring ripple generation. The mice were habituated to head
258 fixation in a tube in a room distinct from the one where imaging experiments were conducted. On
259 the imaging day, the mice were introduced to the recording room and head-fixed under the
260 microscope for the first time.
261
262 CA1PCs were labeled *in utero* on embryonic day (E) 14.5 (*n*=56 cells from 3 sessions in 3 mice) and
263 E17.5 (*n*=55 cells from 3 sessions in 3 mice) and imaged in adult brains. Both neuronal populations

264 exhibited prominent peaks in their grand average CCGs and significantly higher synchronous event
265 rates compared to jittered data (Figure 3-figure supplement 2A, B). Approximately 40% of the
266 recorded neurons participated in synchronous ensembles, indicating robust synchronous activity
267 involving a substantial proportion of the recorded cells (Figure 3-figure supplement 2C).
268
269 In total, 1052 synchronous ensembles and 174 ripple episodes were detected across these imaging
270 sessions. Consistent with findings from walking animals, few synchronous ensembles occurred
271 during ripples when animals were immobilized in a tube (Figure 3-figure supplement 3A, B).
272 Moreover, no distinguishable ripple oscillations were observed in synchronous events, and the
273 average firing rates during ripple episodes were near zero (Figure 3-figure supplement 3C, D). At the
274 single-cell level, 90% of neurons showed significant negative spiking modulation during ripples, with
275 ripple modulation indexes close to -1, indicating strong suppression of spiking (Figure 4Ai). This
276 suppression extended to subthreshold membrane potentials, as nearly all cells exhibited decreased
277 fluorescence during ripples compared to baseline (Figure 4Bi, Ci). These results demonstrate that
278 spiking activity and subthreshold membrane potentials are robustly suppressed during ripples.
279
280 Contextual novelty plays a critical role in shaping hippocampal neuronal activities[40-46]. To assess its
281 influence, we trained mice to become familiar with the imaging procedure and the recording
282 environment over five days and recorded CA1PC activities on the final day. Mean firing rates were
283 significantly reduced in the familiar group compared to the novel group (Familiar group: 1.1 to 5.2
284 Hz (25th-75th percentiles), median=2.3 Hz, n=66 cells, 6 sessions, 4 mice; Novel group: 1.7 to 6.0 Hz
285 (25th-75th percentiles), median=4.2 Hz, n=111 cells, 6 sessions, 6 mice, p=0.0083, Wilcoxon signed-
286 rank test). Additionally, 15% of the neurons in the familiar group exhibited significantly positive
287 spiking modulation by ripples, while fewer cells showed negative modulation compared to the novel
288 group (Figure 4A). During ripples, neurons in the novel group predominantly displayed
289 hyperpolarizing membrane voltage responses, whereas a subset of neurons in the familiar group

exhibited prominent depolarizing responses (Figure 4B). The mean fluorescence changes in the familiar group shifted toward depolarization compared to the novel group (Figure 4C). Finally, synchronous event frequencies were significantly lower in the familiar context, indicating weaker synchronous activities under familiar conditions (Figure 4D). These results demonstrate that hippocampal neuronal activities, particularly synchronous ensembles, are strongly influenced by contextual novelty.

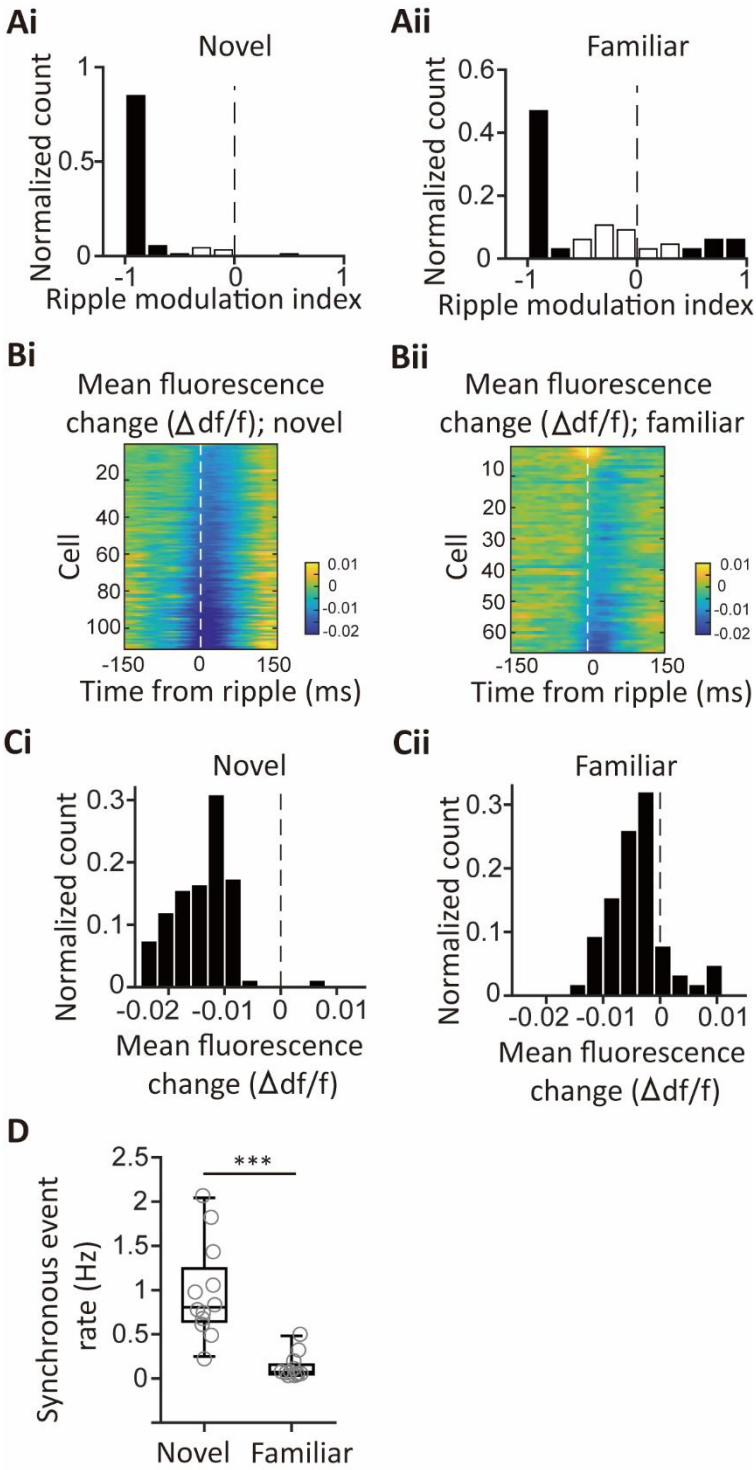

Figure 4. Comparison of ripple-associated neuronal activities and synchronous event rates between novel and familiar recording contexts.

(A) Histograms of ripple modulation indices for the novel (Ai) and familiar (Aii) recording contexts. Gray bars represent modulation indices with significant *p*-values, while white bars indicate non-significant modulation indices.

(B) Color-coded representations of mean fluorescence changes relative to baseline fluorescence for individual neurons, averaged across ripple events, in the novel (Bi) and familiar (Bii) recording contexts.

(C) Histograms of mean fluorescence changes within a ±10-ms window centered on the peak power of ripple events. Ci corresponds to the novel context, while Cii corresponds to the familiar context.

(D) Boxplots of synchronous event rates for the novel and familiar recording contexts. Mean event rates were 0.98±0.16 Hz for the novel context and 0.13±0.04 Hz for the familiar context ($t(22)=5.20$, $p<0.001$, Student's *t*-test). ***$p<0.001$

Synchronous ensembles are associated with theta oscillations

To compare the network dynamics associated with synchronous ensembles during immobility and locomotion, we aligned LFP traces triggered to the timings of synchronous ensembles. The average LFP traces of a representative session showed prominent theta oscillations around the timings of both immobility and locomotion population synchrony (Figure 5A). Spectral analysis of the mean synchrony-triggered LFP traces during immobility and locomotion revealed theta frequency components of 4-12 Hz, with a slightly higher peak frequency in locomotion LFP compared to immobility LFP (Figure 5B). Furthermore, we computed LFP theta modulation and identified preferred phases of synchronous ensembles. In line with the previous result, synchronous ensembles displayed a high level of modulation by LFP theta oscillation (modulation strength: 0.61± 0.05 during immobility and 0.74±0.04 during locomotion, n=5 sessions). Although the preferred phases varied from session to session due to differences in recording sites along the proximal-distal axis of the hippocampus, the timings of individual ensembles were consistently locked to the preferred phase of each session (Figure 5C). These results establish a strong link between synchronous ensembles and LFP theta oscillation.

329 Subthreshold membrane voltage (subVm) is one of the critical parameters supporting the
330 generation of action potentials. To investigate the subthreshold signals underlying population
331 synchrony, we aligned subVm traces with the timings of synchronous ensembles and observed that
332 both immobility and locomotion synchrony rode on a subVm waveform oscillating at theta
333 frequency (Figure 5D). To elucidate further the relationship between subVm theta oscillation and
334 spikes involved in population synchrony, we calculated the subVm theta modulation and preferred
335 phases of spikes. Spikes participating in both immobility and locomotion synchrony were strongly
336 coupled to the subVm theta oscillation of neurons, with the mean preferred phase being in the
337 latter half of the rising phase closer to subVm theta peaks (Figure 5E). Conversely, spikes not
338 participating in synchronous ensembles had weaker modulation strength compared to spikes
339 involved in synchrony (Figure 5-figure supplement 1A, B). Furthermore, the membrane voltages
340 triggered by these two categories of spikes showed a significant difference in the hyperpolarization
341 phase of the theta oscillation. Synchronous spikes were situated within cycles of theta oscillations
342 featuring more hyperpolarized troughs than spikes outside synchronous ensembles (Figure 5-figure
343 supplement 1C, D). Thus, compared to spikes not participating in synchronous ensembles,
344 synchronous spikes showed a more robust modulation by theta oscillation of membrane voltage
345 during immobility and locomotion in the context of novel exploration.
346
347 Notably, phase locking of spikes to their subVm theta oscillation and the synchronous spikes among
348 many neurons suggest that subVms of different neurons would be correlated at the theta frequency.
349 To explore the possibility, we divided the 180-second subVm traces into 1-second segments with
350 50% overlap and calculated the cross-correlation and magnitude-squared coherence function for
351 each pair of cell segments. Segments were sorted into the immobility or locomotion group based on
352 the animals' speed during each segment (kept below 1 cm/s for immobility and above 3 cm/s for
353 locomotion for more than 90% of the time). In total, we analyzed 511 cell pairs from 5 sessions.
354 Indeed, the cross-correlation of subVm between cell pairs revealed a high correlation at zero lag and

355 periodic modulation of the correlation at theta frequency (Figure 5F). Furthermore, the subVm
356 theta coherences were increased in both groups (immobility: 0.50, locomotion: 0.40, median, *n*=511
357 pairs) and were negatively correlated with soma distances (immobility: -0.46, locomotion: -0.48,
358 *n*=511 pairs, Figure 5G). Taken together, during novel exploration, CA1PCs generate synchronous
359 activity associated with theta oscillation and exhibit correlated and theta-coherent subVms.
360
361 Correlated intracellular theta and theta-phase locking of the synchronous ensembles raise the
362 question of whether population synchrony among CA1PCs extends beyond synchrony derived from
363 these effects. To address this, we analyzed population synchrony after randomizing the theta cycles
364 during which neurons spiked, while keeping their theta phases unchanged. Supplementary Figure 4
365 illustrates a significant reduction in synchronous event rates following theta cycle randomization.
366 The finding indicates spiking at specific theta cycles plays a major role in driving population
367 synchrony.
368
369 To further investigate synchronous ensembles across different datasets, we analyzed publicly
370 available hippocampal recordings 'hc-11' from the CRCNS repository[46,47], where rats navigated novel
371 mazes for water rewards (see Method). Using our algorithm, we identified a significant number of
372 synchronous ensembles during the first three minutes of novel navigation. On average, the rates of
373 synchronous events were 6.4-fold higher than those detected in jittered controls (mean event rate:
374 2.0 ± 0.3 Hz for the original data vs. 0.32 ± 0.03 Hz for jittered data, n = 8 sessions, p = 0.0078, W =
375 36, Wilcoxon signed-rank test; Supplementary Figure 5A). To assess whether ripple oscillations were
376 associated with these synchronous ensembles, we analyzed ripple event rates and their relationship
377 to population synchrony. During this period, ripple events were infrequent (mean ripple rate: 0.02 ±
378 0.01, n = 8 sessions), and ripple power peaked during ripple episodes but remained low at the
379 timings of population synchrony (Supplementary Figure 5B). Nevertheless, LFP traces aligned to
380 population synchrony revealed prominent theta oscillations (Supplementary Figure 5C).

Synchronous ensembles were modulated by LFP theta oscillation (modulation strength: 0.30 ± 0.04, n = 8 sessions, $p < 0.001$), and the timings of individual ensembles were consistently locked to the preferred phase of each session, suggesting a functional coupling of synchronous ensembles to theta oscillations important for information processing (Supplementary Figure 5D).

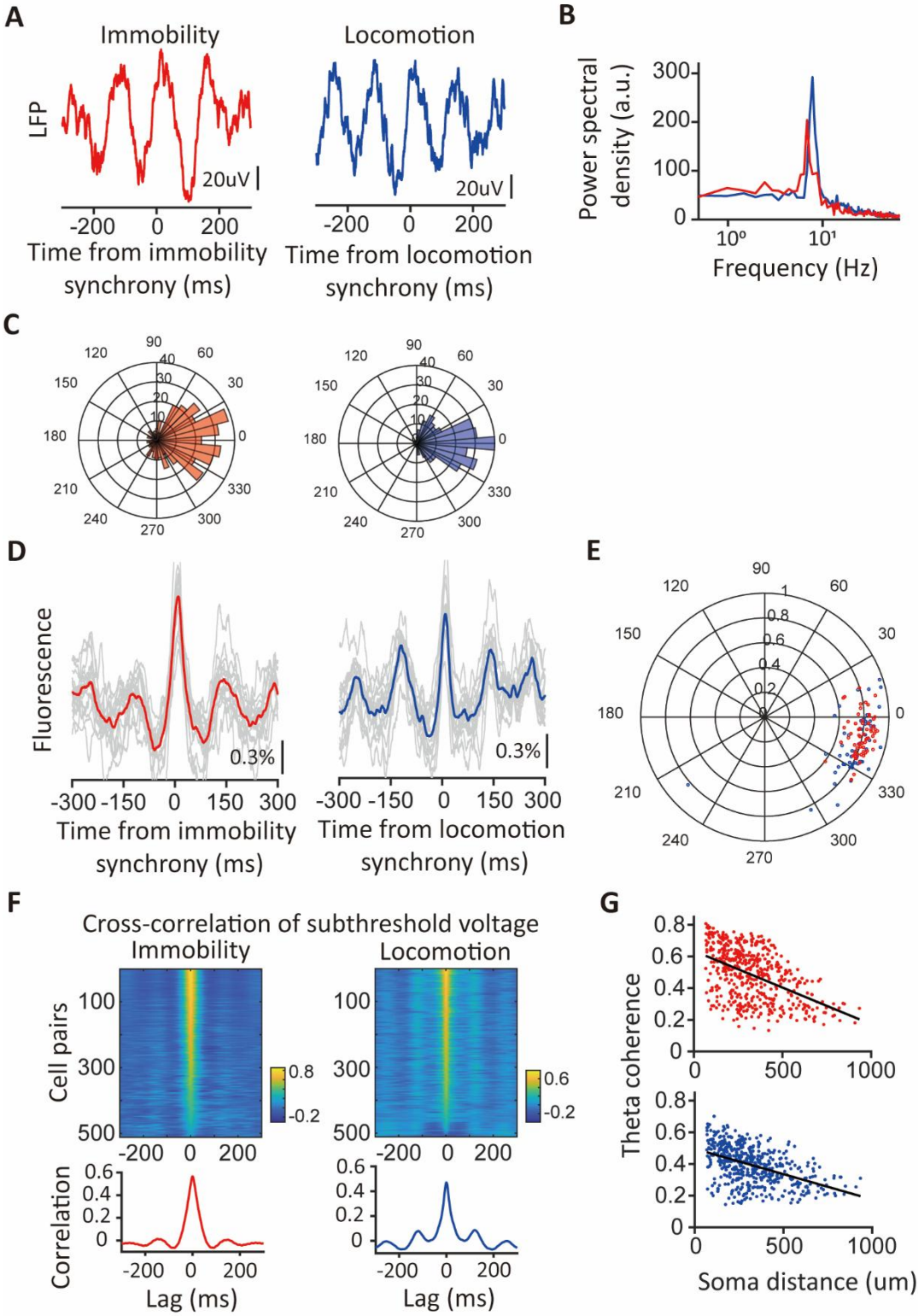

Figure 5. Theta oscillations in the LFP and subthreshold membrane potential were linked to population synchrony.

(A) LFP waveforms triggered by timings of synchronous ensembles. Red: triggered by timings of immobility synchrony; blue: triggered by timings of locomotion synchrony.

(B) Power spectral densities of the triggered LFP waveforms. Red: immobility; blue: locomotion.

(C) Distributions of the differences between LFP theta phases of individual synchronous ensembles and their preferred phases of the session. Note that most ensembles show minor differences within ±30 degrees. Red: immobility; blue: locomotion.

(D) Fluorescence traces triggered by timings of synchronous ensembles. Traces with spikes are excluded. Left panel: traces triggered by timings of immobility synchrony. Right panel: traces triggered by timings of locomotion synchrony. Thin gray lines: mean triggered fluorescence traces averaged across triggers for representative cells. Thick red and blue lines: mean triggered fluorescence traces averaged across cells.

(E) Polar plot illustrating theta modulation of spikes participating in the immobility synchrony (red dots) and of spikes participating in the locomotion synchrony (blue dots). The angle of the dots indicates the preferred phase, and the distance from the center of the circle represents the modulation strength. Each dot represents the averages from a neuron.

(F) Pairwise cross-correlation of the subthreshold membrane voltages (subVm). Top: color-coded cross-correlation of subVm between cell pairs during immobility and locomotion periods. Bottom: averaged cross-correlation over all cell pairs for immobility (red) and locomotion (blue) subVm. Both show a central peak at zero lag flanked by theta oscillation.

(G) Scatter plots of theta coherence against soma distances of immobility subVm (red) and locomotion subVm (blue) between cell pairs.

410 **Synchrony between place cells with distinct place tunings**

411 When animals explore a novel maze, spatially tuned spiking activity can form within a few
412 minutes[48,49]. However, how synchronous ensembles organize their spatially tuned activities during
413 novel exploration remains to be determined. Synchronous ensembles, generating spikes
414 coincidently in short intervals, might display correlated spiking at longer time windows that match
415 behavioral timescales of exploration, potentially leading to shared place responses. On the other
416 hand, CA1PCs are interconnected through inhibitory interneurons[50-52]. Modulation of activities in
417 inhibitory interneurons by some place cells may influence the activities of other place cells,
418 resulting in divergent spatial tunings[48,53,54].

419

420 To compare the spatial tunings of synchronous cell pairs, we first calculated the spatial tuning
421 curves of individual neurons by computing the mean firing rates in every spatial bin. On average,
422 40% of cells displayed selective spatial tunings of their spiking activities and were qualified as place
423 cells[55] (Figure 6A). Among place cell pairs, some showed similar spatial tunings, while others did not
424 (Figure 6B). For instance, in an illustrative session depicted in Figure 6B, the seventh and eighth
425 place cells had highly similar spatial tunings with a correlation coefficient as high as 0.7. In contrast,
426 the fifth and tenth place cells exhibited vastly different spatial tunings with a correlation coefficient
427 as low as -0.5.

428

429 We further explored the relationship between the similarity of spatial tunings and synchronization
430 strength among pairs of place cells. We measured synchronization strength as the peak of the CCG
431 normalized by the averaged jittered spike count within the same bin as the CCG peak. We
432 segregated spikes based on these behavioral states to accommodate differences between
433 locomotion and immobility and calculated the corresponding CCG and synchronization strength.

434

435 During locomotion, we observed a robust negative correlation between synchronization strength

436 and the similarity of spatial tunings among cell pairs. In other words, cell pairs with more precisely
437 co-active spikes during locomotion exhibited more distinct place-tuning profiles (Figure 6C, D). This
438 anti-correlation between synchronization strength and place tunings indicates coordination
439 between place cells' temporal and spatial coding. On the other hand, synchronization strength
440 during immobility showed little correlation with the similarity of spatial tunings among place cell
441 pairs, suggesting that correlated activities at the millisecond timescale do not extend to slow,
442 behavioral-relevant timescales (Figure 6-figure supplement 1). Thus, place cells with distinct place
443 fields are linked by synchronous activity during novel locomotion.
444

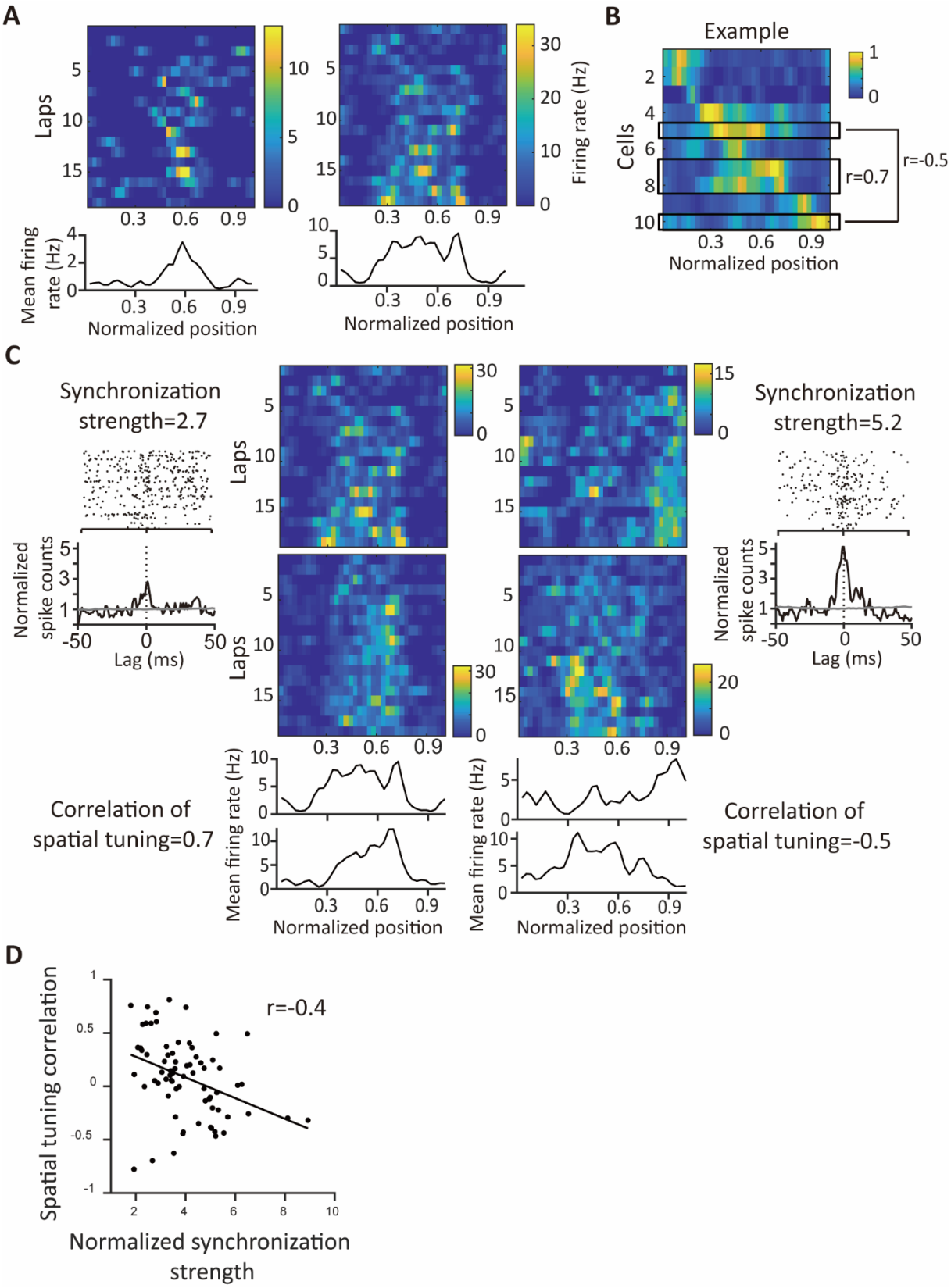

Figure 6. Negative correlation between spatial tuning similarity and synchronization strength during novel exploration.

448 **(A)** Spatially binned rate maps of place cells. High firing rates are indicated in yellow, and low firing
449 rates are noted in blue. Bottom: the mean firing rates along spatial bins averaged across laps.
450 **(B)** Spatial tunings of 10 place cells from an example session. Cells are sorted based on the locations
451 of their peak firing rates.
452 **(C)** Two example pairs of neurons with cross correlograms during locomotion and spatially binned
453 firing rate maps.
454 **(D)** A scatter plot of correlation coefficients of spatial tunings against normalized synchronization
455 strengths for place cell pairs. Each dot represents a pair of place cells. Synchronization strengths are
456 negatively correlated with similarities of spatial tunings (Spearman correlation coefficient=-0.4,
457 $p<0.001$, $n=73$ pairs).
458
459

460 ## Discussion

461 Our findings reveal the presence of synchronous ensembles comprising a substantial number of
462 CA1PCs during both locomotion and immobility in a novel environment. These ensembles
463 concurrently engage neurons representing diverse aspects of the environment and are rarely
464 observed during ripple events. Instead, they closely align with LFP and intracellular theta
465 oscillations. Our data demonstrate theta-associated synchronous ensembles during spatial memory
466 acquisition, coordinating numerous CA1 place cells that transmit information about different
467 segments of the environment.
468
469 The correlation between observed population synchrony and theta oscillations is intriguing. Theta
470 oscillations are typically associated with the sequential activation of neurons over time, resulting in
471 reduced neuronal synchrony[22]. However, theta oscillations come in different types, each
472 characterized by distinct pharmacological properties and behavioral correlates[56-58]. For example,
473 type 1 theta, or translational theta, occurs during voluntary movements and is sensitive to N-

methyl-D-aspartate receptor (NMDAR) blockers. On the other hand, type 2 theta, or attentional theta, is slightly slower and is blocked by muscarinic receptor antagonists, emerging during states of arousal or attention, such as when entering a new environment[59-61]. Consistent with these distinctions, the peak of the power spectrum density shows a distinctively slower theta frequency during immobility compared to locomotion (Figure 5B).

During theta oscillations, cholinergic neurons in the medial septum excite downstream CA1PCs, leading to increased firing rates and membrane potentials[62-64]. Given the widespread influence of cholinergic inputs on numerous CA1PCs, theta-coupled cholinergic inputs may drive depolarization and firing across many CA1PCs. Additionally, they could enhance the likelihood of synchronicity. Furthermore, GABAergic neurons in the medial septum, activated during theta oscillations, could activate interneurons in the CA1 region[58,65,66]. These CA1 interneurons, in turn, have the capability to entrain the activities of pyramidal neurons at both sub- and suprathreshold levels, thereby promoting synchronization among pyramidal neurons[67,68]. In summary, cholinergic and GABAergic neuron activation during theta waves may contribute to the excitation of CA1PCs and the consequent increase in their synchronicity.

Theta oscillations have long been implicated in memory acquisition. Specifically, theta power correlates positively with learning performance[69-71]. Perturbing generation of theta waves leads to impairment in memory acquisition[72-76], while electrical stimulation restoring theta rhythms rescues learning performance[77,78]. Furthermore, increased spike-theta coherence correlates with better memory, and stimulations that boost theta phase-locking of spikes enhance memory[79-81]. Despite abundant evidence supporting a link between theta oscillations and memory, the precise network mechanism by which theta oscillations support memory acquisition remains unclear. Theta oscillations are hypothesized to link spatially distributed neurons into functional ensembles to support memory acquisition[13]. The identified synchronous ensembles support the hypothesis,

500 providing a network substrate that links theta rhythms to the initial stage of memory acquisition.
501
502 Recent studies have demonstrated elevated coactivity of hippocampal principal cells during theta-
503 associated dentate spikes, events that are temporally coupled to theta oscillations and distinct from
504 sharp-wave ripples[82-84]. These findings highlight a network state characterized by rich synchronous
505 ensembles associated with theta, but not ripple, oscillations-a pattern consistent with our results.
506 Our analyses of publicly available data further support these observations, revealing theta-
507 associated population synchrony in a different dataset (Supplementary Figure 5). These results
508 suggest that hippocampal neurons achieve synchrony through network mechanisms distinct from
509 ripple-related events, reinforcing the hypothesis that this phenomenon is generalizable across
510 experimental conditions and behavioral contexts.
511
512 Previous studies have reported that a small percentage of CA1PCs generate spikes during ripple
513 episodes[8,14,17]. These measurements are typically conducted in familiar environments. In contrast,
514 when animals are introduced to a novel environment, ripple-associated spiking activities are
515 strongly suppressed, and CA1PCs exhibit prominent hyperpolarizing responses in their membrane
516 potentials (Figure 3, 4Ai-Ci, and Figure 3-figure supplement 3). Interestingly, after familiarization
517 training, a larger proportion of CA1PCs display positive ripple modulation of spiking activities and
518 depolarizing responses associated with ripples (Figure 4Aii-Cii). Consistent with the observation of
519 ripple-associated spiking activity in familiar environments, our study underscores the influence of
520 contextual novelty on hippocampal dynamics. Specifically, brain states associated with novelty may
521 modulate the activity of neurons upstream of CA1PCs, driving their membrane potentials toward
522 hyperpolarization during ripples. While the reduced correlation between ripples and spikes in novel
523 environments may initially appear counterintuitive, this unique neuronal activity pattern likely
524 reflects adaptive changes in hippocampal circuits related to the animals' behavioral states, such as
525 heightened vigilance in novel environments.

While contralateral LFP recordings reliably capture large-scale hippocampal theta and ripple oscillations[29-31], they may not fully account for ipsilateral-specific dynamics, such as variations in theta phase alignment or locally generated ripple events. Although contralateral recordings serve as a well-established proxy for large-scale hippocampal oscillatory states[30,85-87], incorporating simultaneous ipsilateral field potential recordings in future studies could refine our understanding of local-global network interactions. Despite these considerations, our findings provide robust evidence for the existence of synchronous neuronal ensembles and their role in coordinating newly formed place cells. These results advance our understanding of how synchronous neuronal ensembles contribute to spatial memory acquisition and hippocampal network coordination.

Although CA1PCs are known to exhibit weaker recurrent connectivity than that of CA3 pyramidal neurons, CA1PCs did communicate through monosynaptic connections[88]. These connections can be dynamically adjusted by the spike-timing-dependent plasticity mechanism[89-91], and therefore could be affected by the transient population synchrony. In addition, CA1PCs are known to communicate through inhibitory interneurons. Multiple pyramidal neurons converge onto a single interneuron, and individual connections are often weak and unreliable[51,92,93]. This connectivity scheme requires multiple pyramidal neurons spiking synchronously within the time window of synaptic integration to effectively activate postsynaptic neurons[51]. Furthermore, population synchrony among CA1PCs may propagate to downstream areas, synchronizing neurons outside the hippocampus. With their large ensemble sizes, these synchronous ensembles may synergistically convey relevant information or reorganize the connectivity of the neuronal networks.

Prior studies in sensory systems have commonly revealed that neurons with synchronous activities typically share similar sensory responses[94,95]. However, the synchronous ensembles we have identified often encompass neurons with distinct preferences for place fields. Pairwise synchrony

552 demonstrates a negative correlation with place field overlap (Figure 6). These findings indicate that
553 synchrony does not necessarily imply similar tunings between neurons. Furthermore, these
554 synchronous ensembles involve place cells encoding different spatial information. Recognizing the
555 crucial role of neuronal synchrony in binding distributed neurons in the brain[3,5], population
556 synchrony may serve as a mechanism to integrate diverse features of the same environment into a
557 cohesive mental map.
558

559 # Methods

560 **Animal**

561 Time-pregnant wild-type C57BL/6J female mice underwent in utero virus injection of CamkII-cre
562 virus (105558-AAV1, Addgene) into the left side of the lateral ventricles. The resulting offspring
563 were raised in a breeding room under controlled temperature and humidity conditions and a 12-
564 hour light/dark cycle (lights on from 7:00 to 19:00). The mice used in the experiments were
565 between 12 and 18 weeks old at the time of the recordings. All surgical procedures, behavioral
566 training, and recording protocols were approved by the NYCU Institutional Animal Care and Use
567 Committee.

568

569 **In-utero virus injection**

570 Time-pregnant mice on embryonic day 14.5 or 17.5 were anesthetized with isoflurane (induction:4-
571 5%; maintenance:1-3%) before surgery. The animals were placed on a heating pad in a supine
572 position to maintain body temperature. Aseptic procedures were implemented to maintain sterile
573 conditions during the surgery. Uterine horns were exposed one at a time using spoons and fingers.
574 Warm and sterile phosphate-buffered saline (PBS) was used to rinse the uterus to prevent it from
575 drying out. Micropipettes loaded with CamkII-cre virus solution were used to inject 0.2 μL of virus
576 suspension into the left side of the lateral ventricle of each embryo. The injection resulted in Cre
577 expression among neurons born on the day of injection, with earlier injection labeling neurons
578 located on the deeper side of the cell layer. The uterine horn was then gently returned to the
579 abdominal cavity. The exact process was repeated to the other uterine horn. After the surgery,
580 ketorolac (6mg/kg) and cefazolin (1g/kg) were administered for two days to minimize pain and
581 inflammation.

582

583 **Cranial window and cannula implantation**

584 The offspring of the mice that had undergone in-utero injection were subjected to chronic
585 hippocampal window surgery when they were between 2 and 4 months old. The animals were
586 initially anesthetized using isoflurane (induction:4-5%; maintenance:1-3%). Topical anesthesia was
587 applied by administering 0.5% lidocaine to the wound margins. After achieving deep anesthesia, an
588 incision was made in the skin, and a circular section of the skull was removed, centered 2 mm
589 caudal and 1.8 mm left to the bregma. Using 30-gauge needles and forceps, the dura was removed
590 from the exposed area, and cortical tissue within the craniotomy was aspirated. A serial dilution
591 experiment was conducted to determine an optimal titer of the virus carrying Voltron2 genes,
592 minimizing cell toxicity, for use in this and in previous imaging experiments[32]. A fine injection
593 pipette (tip diameter 10-60 um) was used to inject AAV2/1-CAG-flex-Voltron2-ST (2.7×10^{12} GC/ml, a
594 generous gift from Dr. Eric Schreiter and the GENIE team at HHMI Janelia Research Campus) into the
595 exposed regions at a depth of 200 μm (up to six injection sites and 100-200 nL of viral
596 suspension). An optical chamber was constructed by placing a cannula with a cover slip attached at
597 the bottom over the craniotomy and sealing it with dental acrylic or C&B Metabond (Sun Medical).
598 A custom-built titanium frame was then cemented to the animal's head using dental acrylic or C&B
599 Metabond. Mice received ketorolac (6mg/kg) and cefazolin (1g/kg) for two days following surgery to
600 minimize pain and inflammation.
601
602 **Behavioral training**
603 After at least two weeks of recovery from the window surgery, the mice underwent behavioral
604 training to ensure they were calm and attentive in the test environment. For mice subjected to
605 imaging experiments where they explored an air-lifted plastic track, the initial training phase
606 involved acclimating the mice to head fixation and treadmill running, which took place over 3-5 days
607 in a separate room distinct from the recording setup. Following this training, the imaging
608 experiments were conducted. On the day designated for imaging, the mice were introduced to the
609 recording room for the first time just before the imaging session. During the imaging experiments,

610 the mice were securely held in a head-fixed position beneath the microscope and on an air-lifted
611 plastic track that rested on an air table (AirLift, Neurotar; Figure 1A). The track was adorned with
612 various shapes of signs to help the mice navigate the track. Subdued blue lighting was provided to
613 illuminate the track. Before the initiation of imaging, the mice were confined in a corner of the track
614 using gates. Subsequently, the gates were opened upon the start of imaging, allowing the mice to
615 explore the new environment during their initial laps (Figure 1A Top view). The Mobile HomeCage
616 tracking system (Neurotar) was used to track the mice's position and speed. During the acquisition
617 of image frames, TTL pulses were sent by the high-speed camera to the Mobile HomeCage tracking
618 system to facilitate data alignment. Mice subjected to imaging experiments with head fixation in a
619 tube were first trained in a separate room, distinct from the recording setup, for 1-2 days to
620 habituate them to the head fixation procedure. Following this training, the mice were introduced to
621 the recording room for the first time immediately before the imaging session. During imaging, the
622 mice were securely positioned in a head-fixation setup within an acrylic tube and remained
623 stationary. To further familiarize the mice with the recording context, the imaging procedure was
624 repeated for 4 days without injecting the JF-HaloTag ligand. On the fifth day, the JF-HaloTag ligand
625 was injected prior to imaging, and voltage imaging was performed following the same procedure as
626 in the previous sessions.
627
628 **Voltage imaging**
629 JF_{552}-HaloTag ligand[96] (a generous gift from Dr. Luke Lavis) was first dissolved in DMSO (20 μl,
630 Sigma) and then diluted in Pluronic™ F-127 (20 μl, P3000MP, Invitrogen) and PBS to achieve a
631 final concentration of 0.83 mM of JF_{552}-HaloTag ligand. The solution was then injected intravenously
632 through the retro-orbital sinus. Imaging sessions were initiated 3 hours after the injection of the
633 JF_{552}-HaloTag ligand. Fluorescence sensors were excited using a 532-nm laser (Opus 532, Laser
634 Quantum) with an excitation filter (FF02-520-28, Semrock), and the emitted light was separated
635 from the excitation light using a dichroic mirror (540lpxr Chroma) and passed through an emission

636 filter (FF01-596183 Semrock). A 16X, 0.8 NA objective (Nikon) was used to collect the emission light
637 which was then imaged on a CMOS camera (DaVinci-1K, RedShirt) with a 50-mm camera lens
638 (Nikkor 50mm f1.2, Nikon) as the tube lens. Images were acquired using Turbo-SM64 (Sci-Measure)
639 at 2kHz with a resolution of 190 x 160 pixels, corresponding to a field of view of 1.4 x 1.2 mm. The
640 number of frames in an image session was set at 360,000, corresponding to a duration of 180
641 seconds per session. Imaging depths ranged between 70 and 170 μm from the window surface,
642 where the CA1 pyramidal neurons were located. Time-lapse images were collected, and image
643 stacks of the same field of view along the z-axis were acquired. The image stacks consisted of 100
644 plans separated by two μm, covering the depth from the window surface to 200 um from the
645 surface.
646
647 **LFP recording**
648 The LFP signal from the contralateral CA1 region of the hippocampus was simultaneously recorded
649 during voltage imaging. To implant the LFP electrode, a small craniotomy was performed at the
650 dorsal CA1 coordinate (2mm caudal and 1.8 mm right to the bregma). A tungsten electrode
651 (#100211, 38 μm in diameter, polyimide insulated, California Fine Wire) was inserted into the
652 dorsal CA1 region, and the wire and pins were cemented in place with dental acrylic. In order to
653 target the CA1 pyramidal layer, the depth of the electrode was controlled and tracked by a
654 micromanipulator (Sutter Instrument, MP-285). Pyramidal layer-specific signatures of the LFP
655 signals, such as complex bursts and high-frequency ripple oscillations, were used to guide the
656 targeting. The electrode location was verified by using tungsten electrodes coated with DiI
657 (Invitrogen™, D282), followed by brain slicing after the recordings. The electrical signal was
658 amplified and filtered (1-1kHz) using a DAM80 amplifier (Word Precision Instruments). The
659 amplified signal was acquired by an I/O device (National Instruments USB-6341) and recorded using
660 WaveSurfer (Adam Taylor, HHMI Janelia Research Campus) at 10 kHz during implantation and
661 TurboSM64 (RedShirt) at 8 kHz during imaging.

662

663 **Imaging somata and dendrites *in vivo* using a two-photon microscope**

664 Immediately after voltage imaging, Voltron-labeled neurons were examined *in vivo* under a two-
665 photon microscope to assess the integrity of their membranes and dendrites. Images were acquired
666 using a two-photon scanning microscope equipped with a femtosecond-pulsed laser (Chameleon,
667 Coherent) and a resonant scanner controlled by ScanImage 4.2 software[97] (http://scanimage.org). A
668 16x water-immersion objective (Nikon, 0.8 NA, 3 mm working distance) was used for imaging. Z-
669 stacks of images (512 x 512 pixels, 600 μm x 600 μm) were collected with excitation light at 800
670 nm. The emission light was separated from the excitation light using a primary dichroic mirror
671 (FF735-Di02-25x36, Semrock), followed by a secondary dichroic mirror (565dclp, Chroma) and an
672 emission filter (FF01-609/57-30-D, Semrock). Each image stack consisted of 100 planes, separated
673 by 2 μm, covering depths from the window surface to 200 um below the surface.

674

675 **Histological processing and quantification of soma depth**

676 Mice with Voltron2$_{552}$ labeling were anesthetized with intraperitoneal injections of ketamine (250
677 mg/kg) and xylazine (25 mg/kg) and transcardially perfused with 4% paraformaldehyde in
678 phosphate-buffered saline (PBS; 2 mL/g). The brains were post-fixed in 4% paraformaldehyde
679 overnight and then washed in PBS. Coronal brain sections, 50 μm thick, were prepared using a
680 VT1200 vibratome (Leica). Sections were mounted with Vectashield mounting medium containing
681 DAPI (VectorLabs) to visualize nuclei. The soma depth of Voltron-labeled cells was measured relative
682 to the border between the *stratum pyramidale* (SP) and the *stratum radiatum*. Depth values were
683 normalized to the thickness of the SP, with larger depth ratios indicating somata located deeper
684 along the radial axis.

685

686 **Voltage imaging preprocessing and spike detection**

687 Fluorescence intensities were corrected for brain movement using rigid registration. Regions of

688 interest (ROIs) were manually selected by grouping pixels that cover individual somata. Previous
689 studies have described and validated the procedure for imaging preprocessing and spike
690 detection[31,32,98]. In short, the fluorescence intensities of individual neurons were calculated by
691 averaging the fluorescence intensities of pixels from the same ROIs. Bleaching was corrected by
692 calculating the baseline fluorescence (F_0) at each time point as an average of the fluorescence
693 intensities within $\pm$0.5 seconds around the time point. The dF/F was calculated as the F_0 minus the
694 fluorescence intensity of the same time point divided by F_0. Positive fluorescence transients were
695 detected to identify spikes from the high-passed dF/F traces created by subtracting the dF/F traces
696 from the median-filtered version with a 5-ms window. To simulate the noise of recordings, high-
697 passed dF/F traces were inverted, and the amplitudes of the transients detected from the inverted
698 traces were used to construct a noise distribution of the spike amplitudes. A threshold was set by
699 comparing the amplitudes of the detected transients with the noise distribution of the spike
700 amplitudes to minimize the sum of type I and type II errors. Spikes were first detected when
701 transients were larger than the threshold. Then, spike amplitudes smaller than half of the top 5%
702 spike amplitudes were excluded. The signal-to-noise ratio (SNR) was calculated for each neuron as a
703 ratio of the averaged spike amplitudes over the standard deviation of the high-passed dF/F traces,
704 excluding points 2 ms before and 4 ms after each detected spike to estimate the quality of the
705 recordings. The crosstalk between ROIs was routinely checked by examining the refractory periods
706 of neurons in auto-correlograms. Only neurons meeting the following criteria were included: (1)
707 SNR larger than 5, (2) full width at half maximum of the spike waveform longer than 0.8 ms, (3)
708 mean spike rates higher than 0.1 Hz, (4) distances between soma pairs at least 70 μm. Sessions
709 with at least nine neurons meeting the selection criteria were used for further analysis.
710

711 **Behavioral states of locomotion and immobility**

712 The periods of locomotion were defined as instances when the animals' speed exceeded 3 cm/s,
713 while periods of immobility were determined as instances when the animals' speed fell below 1

714 cm/s.

715

716 **Mean firing rates during locomotion and immobility**

717 To calculate the mean firing rates during locomotion, we counted the number of spikes during
718 locomotion periods and divided this number by the total duration of locomotion. Similarly, for mean
719 firing rates during immobility, we calculated the number of spikes that occurred during immobility
720 periods and divided this number by the total duration of immobility.

721

722 **Correlation between instantaneous firing rate and animal speed**

723 To estimate the instantaneous firing rates of individual neurons over time, we convolved their spike
724 trains with a Gaussian window of 250 ms. Subsequently, we calculated the Pearson correlation
725 coefficient between these instantaneous firing rates and the animal's speed for each neuron.

726

727 **Grand average cross-correlogram (CCG)**

728 Grand average CCGs were generated by constructing histograms of relative spike timings between
729 spikes of a reference cell and spikes of all other neurons in the same session as the target cell
730 population. Histograms were binned using 1-ms time bins. Spike counts were normalized by the
731 number of reference spikes times the number of all other neurons. An equal number of cells from
732 different sessions were randomly selected to form the shuffled target cell population to assess the
733 statistical significance of the CCG peaks. Subsequently, grand average CCGs were computed using
734 shuffled spike trains for comparison. Grand average CCGs were calculated using all spikes in the 180-
735 s recording periods, subsets of spikes during immobility periods (immobility grand average CCGs),
736 and subsets of spikes during locomotion periods (locomotion grand average CCGs).

737

738 **Detection of the population synchrony**

739 To assess population synchrony, we counted the number of spikes from all neurons within a sliding

740 window of 25 ms. To test the significance of the synchrony, we generated surrogate data by jittering
741 spike timings within a ±75-ms window 500 times. The means and standard deviations of each
742 sample point were calculated over the jitter population. Population synchrony was detected as
743 peaks when the spike count in the original data exceeded the mean plus four standard deviations of
744 the spike counts in the jittered data. Synchrony was also evaluated in modified spike trains,
745 including those where later spikes in bursts were removed and those where spike times were
746 shuffled across theta cycles while preserving phases. To estimate synchronous event rates, we
747 divided the entire 180-second recordings into halves and calculated the event rate in each of the 90-
748 s segments. Additionally, ensemble sizes were quantified by counting the percentage of neurons
749 participating in each synchronous event.
750 To detect population synchrony in a publicly available dataset, we analyzed the "hc-11" dataset
751 from CRCNS, which contains hippocampal recordings from rats running on novel mazes for water
752 rewards at designated locations[46,47]. Spikes recorded during the first three minutes of the novel-
753 maze running epochs were used to identify synchronous ensembles and generate jittered control
754 data. Spike counts for both the original and jittered data were calculated using a sliding 25-ms
755 window. The algorithm for testing the significance of synchrony was the same as described above.
756 Synchronous event rates were estimated using the entire 3-minute spike trains for both the original
757 and jittered data.
758
759 **Pairwise cross-correlogram (CCG) of neuronal pairs**
760 To compute the CCG, we first determined the time difference between spikes in the target and
761 reference neurons and then binned these values into 1-ms time bins. CCGs were only computed for
762 pairs with more than 100 counts within the CCG window of ±500 ms to ensure reliable correlation.
763 We defined the peak of the CCG as the local maxima within ±30 ms of lag. To assess the significance
764 of cross-correlations, we generated surrogate data by jittering the spike times of the target neuron

765 within a ±75 ms window. We computed the CCG peak for a thousand iterations and calculated p-
766 values by comparing the percentile of the peak in the null distribution of the jittered peak values.
767 The synchronization strength was estimated as the ratio between the original CCG peak and the
768 mean spike count of the same bin as the original CCG peak averaged across the jittered histograms.
769 For display purposes, the CCGs were smoothed using a 5-point moving average. CCGs were
770 calculated using all spikes in the 180-s recording periods, subsets of spikes during immobility
771 periods (immobility pairwise CCGs), and subsets of spikes during locomotion periods (locomotion
772 pairwise CCGs).
773
774 **LFP ripple analysis**
775 To detect ripples, we performed band-pass filtering of the LFP signal between 120 and 240 Hz,
776 followed by computing the envelope using the absolute values of the Hilbert transform, which was
777 then low-pass filtered at 20 Hz. The start and end times of ripples were identified by setting the
778 upper and lower thresholds at the mean plus 7 and 3.5 times the standard deviation of the
779 envelope, respectively. For a ripple event to be included, three conditions had to be met: (1) values
780 within the event were higher than the lower threshold, (2) at least one value exceeded the upper
781 threshold, and (3) the minimum duration of the event was 30 ms. The start and end times of a
782 ripple event were defined as the positive and negative crossings of the lower threshold,
783 respectively. We defined in-ripple periods as the time between the start and end of detected LFP
784 ripple events, while out-ripple periods were periods outside the in-ripple periods. The envelope
785 peak values of the detected ripple events were used as the time of ripple occurrence. These timings
786 were utilized as trigger timings to calculate averages triggered by ripples. Two co-occurrences were
787 quantified: the percentages of LFP ripple oscillations that occurred with synchronous ensembles
788 and the percentages of synchronous ensembles that occurred with LFP ripple oscillations. The same
789 ripple detection algorithm was applied to the hc-11 dataset. To account for artifacts in the
790 recordings, raw traces and power spectra of the detected events were plotted and inspected for

false positives.

Ripple modulation index

We utilized the ripple modulation index to assess changes in firing rates during ripples compared to periods outside ripples. This index was computed as the ratio of the difference in mean firing rates during in- and out-ripple periods to the sum of the mean firing rates during both periods. Specifically, we first calculated the mean firing rate during in-ripple periods and the mean firing rate during out-ripple periods. Next, we subtracted the mean firing rate during out-ripple periods from the mean firing rate during in-ripple periods and divided the result by the sum of the mean firing rates during both periods. The resulting ripple modulation index indicates the magnitude and direction of the firing rate modulation during ripple compared to periods outside ripples. To assess the significance of the modulation index, we shuffled the spike timings and repeated the calculation a thousand times to generate a distribution of modulation indices from the shuffled data. The original modulation index was then compared to this distribution, and its significance was determined if it exceeded the 95% confidence level of the shuffled indices.

LFP traces triggered by population synchrony and analysis

The midpoints of the synchronous event intervals were utilized as triggers to align LFP traces from both our recordings and the hc-11 dataset. These traces were aligned within a ± 1-second window around the trigger time points. To calculate the spectral density functions of the aligned LFP traces, we performed a 16,384-point fast Fourier transform of the 2-second LFP traces. The power spectra were then estimated as the squared absolute values of the Fourier coefficients. Ripple power was calculated as the sum of the power distributed between 120 and 240 Hz. To calculate theta modulation strength and preferred angles of the synchronous ensembles, LFP was first filtered within the theta frequency range. Then, the phase $\varphi(t)$ and the instantaneous amplitude $A(t)$ of

the filtered LFP were computed using the Hilbert transform. A vector $V_k = A(t_k)e^{i\varphi(t_k)}$ was assigned to each synchronous ensemble that occurred at time t_k. The modulation strength and the preferred phase angle were determined as the absolute value and the phase angle of the summed vector over all ensembles, respectively. Modulation strengths were normalized by the total length of all vectors.

Subthreshold membrane voltage (subVm)

To compute the subVm of individual neurons, we began by determining the difference between the raw dF/F signal and the high-pass version of dF/F. Next, we calculated the spike threshold for each cell by identifying the voltage value corresponding to the peak of the first derivative of the spike waveforms. Any fluorescence values in the slow dF/F time courses that surpassed the spike thresholds were linearly interpolated.

SubVm traces triggered by population synchrony

The midpoint of the time intervals, during which synchronous ensembles were detected, served as the reference points for aligning fluorescence traces within a $\pm$300 ms window around those reference points. To eliminate any interference from membrane potential fluctuations associated with spikes, we excluded aligned traces in cases where any spike occurred within the time intervals of the aligned traces.

SubVm theta modulation and phase preference of spikes occurred inside and outside the population synchrony events

The subVm was initially filtered within the theta frequency range. Subsequently, the phase $\varphi(t)$ and the instantaneous amplitude $A(t)$ of the filtered subVm were computed using the Hilbert transform. Spikes were categorized into four groups: those occurring during or outside immobility synchronous events and those occurring during or outside locomotion synchronous events. Within

each category, a vector $V_k = A(t_k)e^{i\varphi(t_k)}$ was assigned to each spike that occurred at time t_k. The modulation strength and preferred phase angle were determined as the absolute value and phase angle, respectively, of the summed vector over all spikes within a category. To facilitate comparison between neurons, modulation strengths were normalized by the total length of all vectors. The significance of the modulation strength was tested by shuffling the spike timings and recalculating the modulation strength a thousand times to generate a distribution based on the shuffled spike timings. The original modulation strength was then compared to the distribution, with significance determined if it exceeded the 95% confidence interval of the shuffled values. Significant modulation strengths were plotted and compared across groups.

Spike-triggered fluorescence traces

We extracted segments of fluorescence traces using a $\pm$300 ms time window centered on the spike timings. To examine variations in fluorescence waveforms triggered by spikes within and outside synchronous events, we categorized the fluorescence traces based on whether the spikes occurred within or outside these events. Subsequently, we performed pairwise comparisons of the fluorescence values from the same neuron, concentrating on spikes occurring during corresponding behavioral states. Neurons with four or fewer triggering events in any of these categories were omitted from the analysis.

Cross-correlation and coherence analysis to the subVm traces

To calculate cross-correlation and theta coherence of subVm between pairs of neurons during locomotion and immobility, we initially divided the 180-second subVm traces into 1-second segments with a 50% overlap. These segments were then categorized into the locomotion group if the animal's speed remained above three cm/s for more than 90% of the time within that segment. Similarly, segments were sorted into the immobility group if the animal's speed remained below one cm/s for more than 90% of the time within that segment. Subsequently, we computed the

868 cross-correlation and magnitude-squared coherence function of frequency for pairs of co-occurred
869 segments belonging to a specific cell pair. Mean cross-correlations of individual cell pairs were
870 averaged across segments that occurred in the same behavioral states (i.e., locomotion or
871 immobility states). To estimate theta coherence, we averaged the values of the coherence function
872 within the theta frequency range (4-12 Hz). Theta coherences from the same cell pair during the
873 same behavioral state were pooled together, and the average was used as an estimate for the theta
874 coherence of that cell pair during a particular behavioral state. Finally, Spearman correlation
875 coefficients were calculated between the mean theta coherences of cell pairs and their soma
876 distances.
877
878 **Spatial analysis**
879 We partitioned a 90-cm-long track into 36 spatial bins to analyze spatial tuning properties. For each
880 cell, the spatial tuning curve was computed by determining the mean firing rate, defined as the
881 number of spikes within the bin when the animal's speed exceeded three cm/s, divided by the total
882 dwell times using the same speed threshold. The peak firing rates were identified as the maximal
883 rate on the spatial tuning curve. Spatial selectivity was calculated as one minus the circular variance
884 of the spatial tuning curve. Neurons were classified as place cells when their spatial selectivity
885 exceeded 0.25, and peak firing rates exceeded 1 Hz. To assess the similarity of spatial tuning
886 between pairs of neurons, Spearman correlation coefficients were calculated for the spatial tuning
887 curves. To explore the relationship between levels of synchronization and spatial tuning similarity
888 among pairs of place cells, Spearman correlation coefficients were computed between
889 synchronization strengths of cell pairs and correlation coefficients of their spatial tuning curves.
890
891 **Data analysis and statistics**
892 Data analysis was performed using MATLAB (Mathworks, R2019b), and results were presented as
893 standard error of the mean unless otherwise specified. Boxplots were used to depict the median,

first quartile, and third quartile, with the middle line, the upper edge, and the lower edge of the box, respectively. The whiskers of the boxplots represented the 5th and 95th percentiles of the distribution.

898 1 Takeuchi, T., Duszkiewicz, A. J. & Morris, R. G. The synaptic plasticity and memory hypothesis:
899 encoding, storage and persistence. *Philos Trans R Soc Lond B Biol Sci* **369**, 20130288 (2014).
900 https://doi.org:10.1098/rstb.2013.0288
901 2 Moser, M. B., Rowland, D. C. & Moser, E. I. Place cells, grid cells, and memory. *Cold Spring Harb*
902 *Perspect Biol* **7**, a021808 (2015). https://doi.org:10.1101/cshperspect.a021808
903 3 Axmacher, N., Mormann, F., Fernandez, G., Elger, C. E. & Fell, J. Memory formation by neuronal
904 synchronization. *Brain Res Rev* **52**, 170-182 (2006).
905 https://doi.org:10.1016/j.brainresrev.2006.01.007
906 4 Paulsen, O. & Sejnowski, T. J. Natural patterns of activity and long-term synaptic plasticity. *Curr*
907 *Opin Neurobiol* **10**, 172-179 (2000). https://doi.org:10.1016/s0959-4388(00)00076-3
908 5 Wang, X. J. Neurophysiological and computational principles of cortical rhythms in cognition.
909 *Physiol Rev* **90**, 1195-1268 (2010). https://doi.org:10.1152/physrev.00035.2008
910 6 Harris, K. D., Csicsvari, J., Hirase, H., Dragoi, G. & Buzsaki, G. Organization of cell assemblies in
911 the hippocampus. *Nature* **424**, 552-556 (2003). https://doi.org:10.1038/nature01834
912 7 Squire, L. R. & Wixted, J. T. The cognitive neuroscience of human memory since H.M. *Annu*
913 *Rev Neurosci* **34**, 259-288 (2011). https://doi.org:10.1146/annurev-neuro-061010-113720
914 8 Buzsaki, G. Hippocampal sharp wave-ripple: A cognitive biomarker for episodic memory and
915 planning. *Hippocampus* **25**, 1073-1188 (2015). https://doi.org:10.1002/hipo.22488
916 9 Nadasdy, Z., Hirase, H., Czurko, A., Csicsvari, J. & Buzsaki, G. Replay and time compression of
917 recurring spike sequences in the hippocampus. *J Neurosci* **19**, 9497-9507 (1999).
918 https://doi.org:10.1523/JNEUROSCI.19-21-09497.1999
919 10 Cheng, S. & Frank, L. M. New experiences enhance coordinated neural activity in the
920 hippocampus. *Neuron* **57**, 303-313 (2008). https://doi.org:10.1016/j.neuron.2007.11.035
921 11 Dragoi, G. & Tonegawa, S. Preplay of future place cell sequences by hippocampal cellular
922 assemblies. *Nature* **469**, 397-401 (2011). https://doi.org:10.1038/nature09633
923 12 Liu, C., Todorova, R., Tang, W., Oliva, A. & Fernandez-Ruiz, A. Associative and predictive
924 hippocampal codes support memory-guided behaviors. *Science* **382**, eadi8237 (2023).
925 https://doi.org:10.1126/science.adi8237
926 13 Colgin, L. L. Rhythms of the hippocampal network. *Nat Rev Neurosci* **17**, 239-249 (2016).
927 https://doi.org:10.1038/nrn.2016.21
928 14 Buzsaki, G. & Silva, F. L. High frequency oscillations in the intact brain. *Prog Neurobiol* **98**, 241-
929 249 (2012). https://doi.org:10.1016/j.pneurobio.2012.02.004
930 15 Csicsvari, J., Hirase, H., Czurko, A. & Buzsaki, G. Reliability and state dependence of pyramidal
931 cell-interneuron synapses in the hippocampus: an ensemble approach in the behaving rat.
932 *Neuron* **21**, 179-189 (1998). https://doi.org:10.1016/s0896-6273(00)80525-5
933 16 Gillespie, A. K. *et al.* Hippocampal replay reflects specific past experiences rather than a plan
934 for subsequent choice. *Neuron* **109**, 3149-3163 e3146 (2021).
935 https://doi.org:10.1016/j.neuron.2021.07.029

17 Yagi, S., Igata, H., Ikegaya, Y. & Sasaki, T. Awake hippocampal synchronous events are incorporated into offline neuronal reactivation. *Cell Rep* **42**, 112871 (2023). https://doi.org:10.1016/j.celrep.2023.112871

18 El-Gaby, M. *et al.* An emergent neural coactivity code for dynamic memory. *Nat Neurosci* **24**, 694-704 (2021). https://doi.org:10.1038/s41593-021-00820-w

19 Skaggs, W. E., McNaughton, B. L., Wilson, M. A. & Barnes, C. A. Theta phase precession in hippocampal neuronal populations and the compression of temporal sequences. *Hippocampus* **6**, 149-172 (1996). https://doi.org:10.1002/(SICI)1098-1063(1996)6:2<149::AID-HIPO6>3.0.CO;2-K

20 Dragoi, G. & Buzsaki, G. Temporal encoding of place sequences by hippocampal cell assemblies. *Neuron* **50**, 145-157 (2006). https://doi.org:10.1016/j.neuron.2006.02.023

21 Foster, D. J. & Wilson, M. A. Hippocampal theta sequences. *Hippocampus* **17**, 1093-1099 (2007). https://doi.org:10.1002/hipo.20345

22 Mizuseki, K. & Buzsaki, G. Theta oscillations decrease spike synchrony in the hippocampus and entorhinal cortex. *Philos Trans R Soc Lond B Biol Sci* **369**, 20120530 (2014). https://doi.org:10.1098/rstb.2012.0530

23 O'Keefe, J. & Recce, M. L. Phase relationship between hippocampal place units and the EEG theta rhythm. *Hippocampus* **3**, 317-330 (1993). https://doi.org:10.1002/hipo.450030307

24 Lee, A. K. & Brecht, M. Elucidating Neuronal Mechanisms Using Intracellular Recordings during Behavior. *Trends Neurosci* **41**, 385-403 (2018). https://doi.org:10.1016/j.tins.2018.03.014

25 Petersen, C. C. H. Whole-Cell Recording of Neuronal Membrane Potential during Behavior. *Neuron* **95**, 1266-1281 (2017). https://doi.org:10.1016/j.neuron.2017.06.049

26 Giocomo, L. M., Zilli, E. A., Fransen, E. & Hasselmo, M. E. Temporal frequency of subthreshold oscillations scales with entorhinal grid cell field spacing. *Science* **315**, 1719-1722 (2007). https://doi.org:10.1126/science.1139207

27 Lampl, I., Reichova, I. & Ferster, D. Synchronous membrane potential fluctuations in neurons of the cat visual cortex. *Neuron* **22**, 361-374 (1999). https://doi.org:10.1016/s0896-6273(00)81096-x

28 Poulet, J. F. & Petersen, C. C. Internal brain state regulates membrane potential synchrony in barrel cortex of behaving mice. *Nature* **454**, 881-885 (2008). https://doi.org:10.1038/nature07150

29 Buzsaki, G. *et al.* Hippocampal network patterns of activity in the mouse. *Neuroscience* **116**, 201-211 (2003). https://doi.org:10.1016/s0306-4522(02)00669-3

30 Szabo, G. G. *et al.* Ripple-selective GABAergic projection cells in the hippocampus. *Neuron* **110**, 1959-1977 e1959 (2022). https://doi.org:10.1016/j.neuron.2022.04.002

31 Huang, Y. C. *et al.* Dynamic assemblies of parvalbumin interneurons in brain oscillations. *Neuron* **112**, 2600-2613 e2605 (2024). https://doi.org:10.1016/j.neuron.2024.05.015

32 Abdelfattah, A. S. *et al.* Sensitivity optimization of a rhodopsin-based fluorescent voltage

indicator. *Neuron* (2023). https://doi.org:10.1016/j.neuron.2023.03.009

33 Angevine Jr, J. B. Time of neuron origin in the hippocampal region: an autoradiographic study in the mouse. *Experimental Neurology* (1965).

34 Bayer, S. A. Development of the hippocampal region in the rat. I. Neurogenesis examined with 3H-thymidine autoradiography. *J Comp Neurol* **190**, 87-114 (1980). https://doi.org:10.1002/cne.901900107

35 Cavalieri, D. *et al.* CA1 pyramidal cell diversity is rooted in the time of neurogenesis. *Elife* **10** (2021). https://doi.org:10.7554/eLife.69270

36 Cembrowski, M. S. *et al.* Spatial Gene-Expression Gradients Underlie Prominent Heterogeneity of CA1 Pyramidal Neurons. *Neuron* **89**, 351-368 (2016). https://doi.org:10.1016/j.neuron.2015.12.013

37 Huszar, R., Zhang, Y., Blockus, H. & Buzsaki, G. Preconfigured dynamics in the hippocampus are guided by embryonic birthdate and rate of neurogenesis. *Nat Neurosci* **25**, 1201-1212 (2022). https://doi.org:10.1038/s41593-022-01138-x

38 Adam, Y. *et al.* Voltage imaging and optogenetics reveal behaviour-dependent changes in hippocampal dynamics. *Nature* **569**, 413-417 (2019). https://doi.org:10.1038/s41586-019-1166-7

39 Klausberger, T. *et al.* Brain-state- and cell-type-specific firing of hippocampal interneurons in vivo. *Nature* **421**, 844-848 (2003). https://doi.org:10.1038/nature01374

40 Wilson, M. A. & McNaughton, B. L. Dynamics of the hippocampal ensemble code for space. *Science* **261**, 1055-1058 (1993).

41 Frank, L. M., Stanley, G. B. & Brown, E. N. Hippocampal plasticity across multiple days of exposure to novel environments. *J Neurosci* **24**, 7681-7689 (2004). https://doi.org:10.1523/JNEUROSCI.1958-04.2004

42 Leutgeb, S., Leutgeb, J. K., Treves, A., Moser, M. B. & Moser, E. I. Distinct ensemble codes in hippocampal areas CA3 and CA1. *Science* **305**, 1295-1298 (2004). https://doi.org:10.1126/science.1100265

43 Nitz, D. & McNaughton, B. Differential modulation of CA1 and dentate gyrus interneurons during exploration of novel environments. *J Neurophysiol* **91**, 863-872 (2004). https://doi.org:10.1152/jn.00614.2003

44 Karlsson, M. P. & Frank, L. M. Network dynamics underlying the formation of sparse, informative representations in the hippocampus. *J Neurosci* **28**, 14271-14281 (2008). https://doi.org:10.1523/JNEUROSCI.4261-08.2008

45 Jeewajee, A., Lever, C., Burton, S., O'Keefe, J. & Burgess, N. Environmental novelty is signaled by reduction of the hippocampal theta frequency. *Hippocampus* **18**, 340-348 (2008). https://doi.org:10.1002/hipo.20394

46 Grosmark, A. D. & Buzsaki, G. Diversity in neural firing dynamics supports both rigid and learned hippocampal sequences. *Science* **351**, 1440-1443 (2016).

https://doi.org:10.1126/science.aad1935

47 Grosmark, A. D., Long, J. & Buzsáki, G. r. Recordings from hippocampal area CA1, PRE, during and POST novel spatial learning. *CRCNS. org* **10**, K0862DC0865 (2016).

48 Rolotti, S. V. *et al.* Local feedback inhibition tightly controls rapid formation of hippocampal place fields. *Neuron* **110**, 783-794 e786 (2022). https://doi.org:10.1016/j.neuron.2021.12.003

49 Sheffield, M. E. J., Adoff, M. D. & Dombeck, D. A. Increased Prevalence of Calcium Transients across the Dendritic Arbor during Place Field Formation. *Neuron* **96**, 490-504 e495 (2017). https://doi.org:10.1016/j.neuron.2017.09.029

50 Takacs, V. T., Klausberger, T., Somogyi, P., Freund, T. F. & Gulyas, A. I. Extrinsic and local glutamatergic inputs of the rat hippocampal CA1 area differentially innervate pyramidal cells and interneurons. *Hippocampus* **22**, 1379-1391 (2012). https://doi.org:10.1002/hipo.20974

51 English, D. F. *et al.* Pyramidal Cell-Interneuron Circuit Architecture and Dynamics in Hippocampal Networks. *Neuron* **96**, 505-520 e507 (2017). https://doi.org:10.1016/j.neuron.2017.09.033

52 Maccaferri, G., Roberts, J. D., Szucs, P., Cottingham, C. A. & Somogyi, P. Cell surface domain specific postsynaptic currents evoked by identified GABAergic neurones in rat hippocampus in vitro. *J Physiol* **524 Pt 1**, 91-116 (2000). https://doi.org:10.1111/j.1469-7793.2000.t01-3-00091.x

53 Geiller, T. *et al.* Local circuit amplification of spatial selectivity in the hippocampus. *Nature* **601**, 105-109 (2022). https://doi.org:10.1038/s41586-021-04169-9

54 Trouche, S. *et al.* Recoding a cocaine-place memory engram to a neutral engram in the hippocampus. *Nat Neurosci* **19**, 564-567 (2016). https://doi.org:10.1038/nn.4250

55 Go, M. A. *et al.* Place Cells in Head-Fixed Mice Navigating a Floating Real-World Environment. *Front Cell Neurosci* **15**, 618658 (2021). https://doi.org:10.3389/fncel.2021.618658

56 Kramis, R., Vanderwolf, C. H. & Bland, B. H. Two types of hippocampal rhythmical slow activity in both the rabbit and the rat: relations to behavior and effects of atropine, diethyl ether, urethane, and pentobarbital. *Exp Neurol* **49**, 58-85 (1975). https://doi.org:10.1016/0014-4886(75)90195-8

57 Bland, B. H. The physiology and pharmacology of hippocampal formation theta rhythms. *Prog Neurobiol* **26**, 1-54 (1986). https://doi.org:10.1016/0301-0082(86)90019-5

58 Buzsaki, G. Theta oscillations in the hippocampus. *Neuron* **33**, 325-340 (2002). https://doi.org:10.1016/s0896-6273(02)00586-x

59 Sainsbury, R. S., Heynen, A. & Montoya, C. P. Behavioral correlates of hippocampal type 2 theta in the rat. *Physiol Behav* **39**, 513-519 (1987). https://doi.org:10.1016/0031-9384(87)90382-9

60 Sainsbury, R. S. Hippocampal theta: a sensory-inhibition theory of function. *Neurosci Biobehav Rev* **22**, 237-241 (1998). https://doi.org:10.1016/s0149-7634(97)00011-0

61 Barry, C., Heys, J. G. & Hasselmo, M. E. Possible role of acetylcholine in regulating spatial novelty effects on theta rhythm and grid cells. *Front Neural Circuits* **6**, 5 (2012).

https://doi.org:10.3389/fncir.2012.00005

62 Nakajima, Y., Nakajima, S., Leonard, R. J. & Yamaguchi, K. Acetylcholine raises excitability by inhibiting the fast transient potassium current in cultured hippocampal neurons. *Proc Natl Acad Sci U S A* **83**, 3022-3026 (1986). https://doi.org:10.1073/pnas.83.9.3022

63 Markram, H. & Segal, M. Acetylcholine potentiates responses to N-methyl-D-aspartate in the rat hippocampus. *Neurosci Lett* **113**, 62-65 (1990). https://doi.org:10.1016/0304-3940(90)90495-u

64 Fraser, D. D. & MacVicar, B. A. Cholinergic-dependent plateau potential in hippocampal CA1 pyramidal neurons. *J Neurosci* **16**, 4113-4128 (1996). https://doi.org:10.1523/JNEUROSCI.16-13-04113.1996

65 Toth, K., Freund, T. F. & Miles, R. Disinhibition of rat hippocampal pyramidal cells by GABAergic afferents from the septum. *J Physiol* **500 (Pt 2)**, 463-474 (1997). https://doi.org:10.1113/jphysiol.1997.sp022033

66 Colgin, L. L. Mechanisms and functions of theta rhythms. *Annu Rev Neurosci* **36**, 295-312 (2013). https://doi.org:10.1146/annurev-neuro-062012-170330

67 Cobb, S. R., Buhl, E. H., Halasy, K., Paulsen, O. & Somogyi, P. Synchronization of neuronal activity in hippocampus by individual GABAergic interneurons. *Nature* **378**, 75-78 (1995). https://doi.org:10.1038/378075a0

68 Stark, E. *et al.* Inhibition-induced theta resonance in cortical circuits. *Neuron* **80**, 1263-1276 (2013). https://doi.org:10.1016/j.neuron.2013.09.033

69 Landfield, P. W., McGaugh, J. L. & Tusa, R. J. Theta rhythm: a temporal correlate of memory storage processes in the rat. *Science* **175**, 87-89 (1972). https://doi.org:10.1126/science.175.4017.87

70 Berry, S. D. & Thompson, R. F. Prediction of learning rate from the hippocampal electroencephalogram. *Science* **200**, 1298-1300 (1978). https://doi.org:10.1126/science.663612

71 Belchior, H., Lopes-Dos-Santos, V., Tort, A. B. & Ribeiro, S. Increase in hippocampal theta oscillations during spatial decision making. *Hippocampus* **24**, 693-702 (2014). https://doi.org:10.1002/hipo.22260

72 Winson, J. Loss of hippocampal theta rhythm results in spatial memory deficit in the rat. *Science* **201**, 160-163 (1978). https://doi.org:10.1126/science.663646

73 Mitchell, S. J., Rawlins, J. N., Steward, O. & Olton, D. S. Medial septal area lesions disrupt theta rhythm and cholinergic staining in medial entorhinal cortex and produce impaired radial arm maze behavior in rats. *J Neurosci* **2**, 292-302 (1982). https://doi.org:10.1523/JNEUROSCI.02-03-00292.1982

74 Mizumori, S. J., Perez, G. M., Alvarado, M. C., Barnes, C. A. & McNaughton, B. L. Reversible inactivation of the medial septum differentially affects two forms of learning in rats. *Brain research* **528**, 12-20 (1990). https://doi.org:10.1016/0006-8993(90)90188-h

75 M'Harzi, M. & Jarrard, L. E. Effects of medial and lateral septal lesions on acquisition of a place and cue radial maze task. *Behav Brain Res* **49**, 159-165 (1992). https://doi.org:10.1016/s0166-4328(05)80160-3

76 Wang, Y., Romani, S., Lustig, B., Leonardo, A. & Pastalkova, E. Theta sequences are essential for internally generated hippocampal firing fields. *Nat Neurosci* **18**, 282-288 (2015). https://doi.org:10.1038/nn.3904

77 McNaughton, N., Ruan, M. & Woodnorth, M. A. Restoring theta-like rhythmicity in rats restores initial learning in the Morris water maze. *Hippocampus* **16**, 1102-1110 (2006). https://doi.org:10.1002/hipo.20235

78 Lee, D. J. *et al.* Medial septal nucleus theta frequency deep brain stimulation improves spatial working memory after traumatic brain injury. *J Neurotrauma* **30**, 131-139 (2013). https://doi.org:10.1089/neu.2012.2646

79 Hasselmo, M. E., Bodelon, C. & Wyble, B. P. A proposed function for hippocampal theta rhythm: separate phases of encoding and retrieval enhance reversal of prior learning. *Neural Comput* **14**, 793-817 (2002). https://doi.org:10.1162/089976602317318965

80 Rutishauser, U., Ross, I. B., Mamelak, A. N. & Schuman, E. M. Human memory strength is predicted by theta-frequency phase-locking of single neurons. *Nature* **464**, 903-907 (2010). https://doi.org:10.1038/nature08860

81 Siegle, J. H. & Wilson, M. A. Enhancement of encoding and retrieval functions through theta phase-specific manipulation of hippocampus. *Elife* **3**, e03061 (2014). https://doi.org:10.7554/eLife.03061

82 McHugh, S. B. *et al.* Offline hippocampal reactivation during dentate spikes supports flexible memory. *Neuron* **112**, 3768-3781 e3768 (2024). https://doi.org:10.1016/j.neuron.2024.08.022

83 Dvorak, D., Chung, A., Park, E. H. & Fenton, A. A. Dentate spikes and external control of hippocampal function. *Cell Rep* **36**, 109497 (2021). https://doi.org:10.1016/j.celrep.2021.109497

84 Farrell, J. S., Hwaun, E., Dudok, B. & Soltesz, I. Neural and behavioural state switching during hippocampal dentate spikes. *Nature* **628**, 590-595 (2024). https://doi.org:10.1038/s41586-024-07192-8

85 Dudok, B. *et al.* Alternating sources of perisomatic inhibition during behavior. *Neuron* **109**, 997-1012 e1019 (2021). https://doi.org:10.1016/j.neuron.2021.01.003

86 Terada, S. *et al.* Adaptive stimulus selection for consolidation in the hippocampus. *Nature* **601**, 240-244 (2022). https://doi.org:10.1038/s41586-021-04118-6

87 Geiller, T. *et al.* Large-Scale 3D Two-Photon Imaging of Molecularly Identified CA1 Interneuron Dynamics in Behaving Mice. *Neuron* **108**, 968-983 e969 (2020). https://doi.org:10.1016/j.neuron.2020.09.013

88 Deuchars, J. & Thomson, A. M. CA1 pyramid-pyramid connections in rat hippocampus in vitro:

dual intracellular recordings with biocytin filling. *Neuroscience* **74**, 1009-1018 (1996). https://doi.org:10.1016/0306-4522(96)00251-5

89 Caporale, N. & Dan, Y. Spike timing-dependent plasticity: a Hebbian learning rule. *Annu Rev Neurosci* **31**, 25-46 (2008). https://doi.org:10.1146/annurev.neuro.31.060407.125639

90 Markram, H., Lubke, J., Frotscher, M. & Sakmann, B. Regulation of synaptic efficacy by coincidence of postsynaptic APs and EPSPs. *Science* **275**, 213-215 (1997). https://doi.org:10.1126/science.275.5297.213

91 Bi, G. Q. & Poo, M. M. Synaptic modifications in cultured hippocampal neurons: dependence on spike timing, synaptic strength, and postsynaptic cell type. *J Neurosci* **18**, 10464-10472 (1998). https://doi.org:10.1523/JNEUROSCI.18-24-10464.1998

92 Ali, A. B., Deuchars, J., Pawelzik, H. & Thomson, A. M. CA1 pyramidal to basket and bistratified cell EPSPs: dual intracellular recordings in rat hippocampal slices. *J Physiol* **507 (Pt 1)**, 201-217 (1998). https://doi.org:10.1111/j.1469-7793.1998.201bu.x

93 Ali, A. B. & Thomson, A. M. Facilitating pyramid to horizontal oriens-alveus interneurone inputs: dual intracellular recordings in slices of rat hippocampus. *J Physiol* **507 (Pt 1)**, 185-199 (1998). https://doi.org:10.1111/j.1469-7793.1998.185bu.x

94 Engel, A. K., Konig, P., Kreiter, A. K. & Singer, W. Interhemispheric synchronization of oscillatory neuronal responses in cat visual cortex. *Science* **252**, 1177-1179 (1991). https://doi.org:10.1126/science.252.5009.1177

95 Alonso, J. M., Usrey, W. M. & Reid, R. C. Precisely correlated firing in cells of the lateral geniculate nucleus. *Nature* **383**, 815-819 (1996). https://doi.org:10.1038/383815a0

96 Zheng, Q. *et al.* Rational Design of Fluorogenic and Spontaneously Blinking Labels for Super-Resolution Imaging. *ACS Cent Sci* **5**, 1602-1613 (2019). https://doi.org:10.1021/acscentsci.9b00676

97 Pologruto, T. A., Sabatini, B. L. & Svoboda, K. ScanImage: flexible software for operating laser scanning microscopes. *Biomed Eng Online* **2**, 13 (2003). https://doi.org:10.1186/1475-925X-2-13

98 Abdelfattah, A. S. *et al.* Bright and photostable chemigenetic indicators for extended in vivo voltage imaging. *Science* **365**, 699-704 (2019). https://doi.org:10.1126/science.aav6416

Acknowledgments

We express our sincere gratitude to Dr. Luke Lavis for sharing the JF_{552}-HaloTag ligand. Special thanks to Mr. Yu-Ting Lin and Ms. Hui-Ching Chen for technical assistance. We are grateful to Drs. Shih-Chieh Lin, Kuo-Hua Huang, Shi-Bing Yang, and Fu-Chin Liu for their insightful comments on the manuscript.

Funding statements

National Science and Technology Council, Taiwan (B.-J.L. and T.-W.C.)

Howard Hughes Medical Institute, USA (E.R.S.)

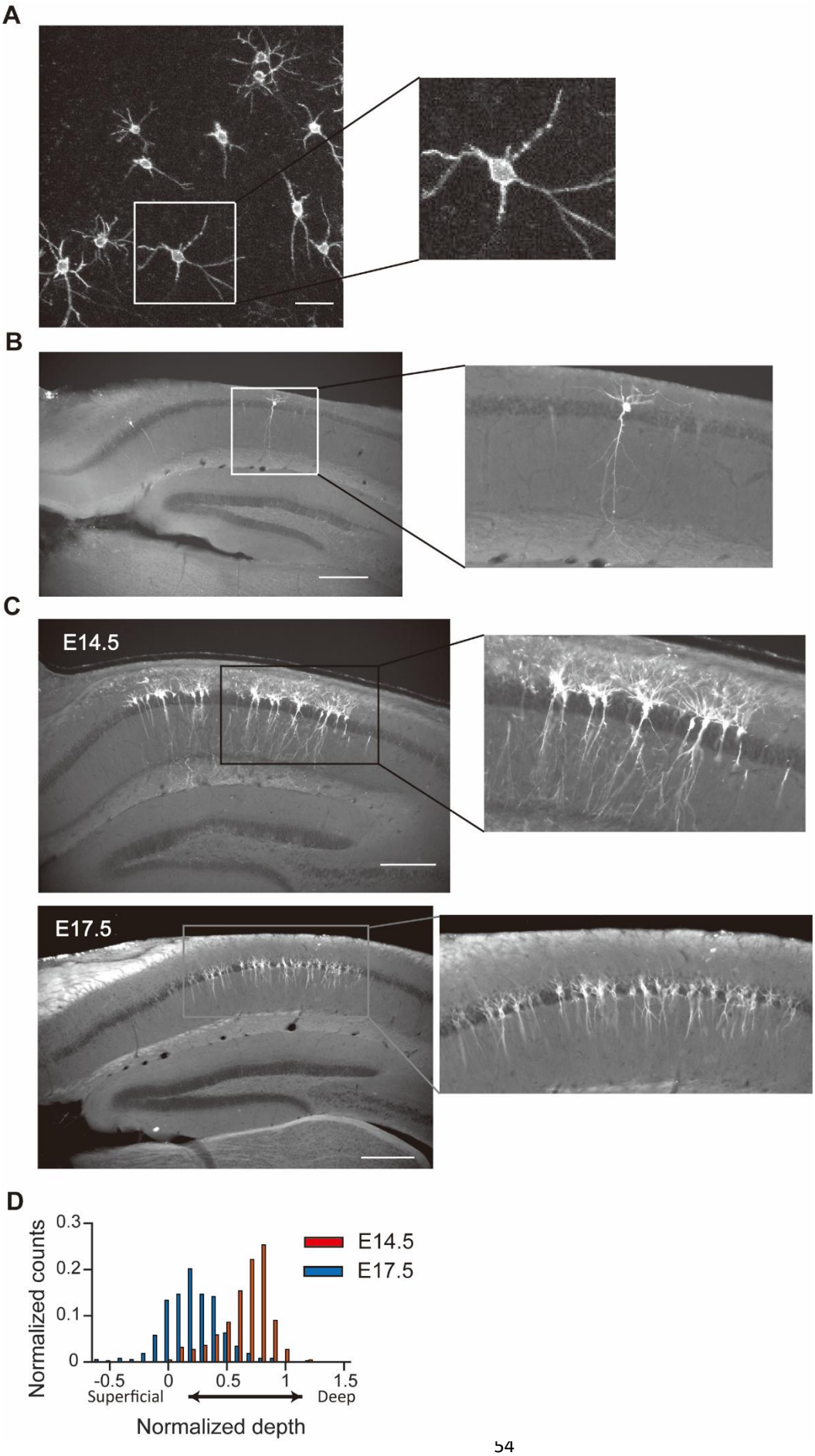
A
B
C
E14.5
E17.5
D
Normalized counts
0.3
0.2
0.1
0
-0.5
0
0.5
1
1.5
Superficial
Deep
Normalized depth
E14.5
E17.5

1166

1167 **Supplementary Figure 1. Morphology of Voltron-expressing neurons and their positions along the**

1168 **deep-superficial axis.**

1169 **(A)** Two-photon z-stack maximum intensity projection images of Voltron-expressing neurons

1170 obtained after imaging experiments. These neurons exhibit well-preserved membrane and dendritic

1171 morphology. Scale bars: 50 μ m.

1172 **(B)** Post-hoc histological images of a sparsely labeled neuron previously subjected to voltage

1173 imaging. Scale bars: 300 μ m.

1174 **(C)** Micrographs of labeled neurons from *in-utero* electroporation at embryonic day 14.5 (E14.5;

1175 upper panel) and E17.5 (lower panel). Scale bars: 300 μ m.

1176 **(D)** Histograms of normalized depths for E14.5 neurons (red) and E17.5 neurons (blue). A higher

1177 normalized depth indicates that the soma is located deeper within the pyramidal layer. Normalized

1178 depths for E14.5 neurons are significantly higher than those for E17.5 neurons ($t_{(601)}$=22.8,

1179 p<0.0001, Student's t-test).

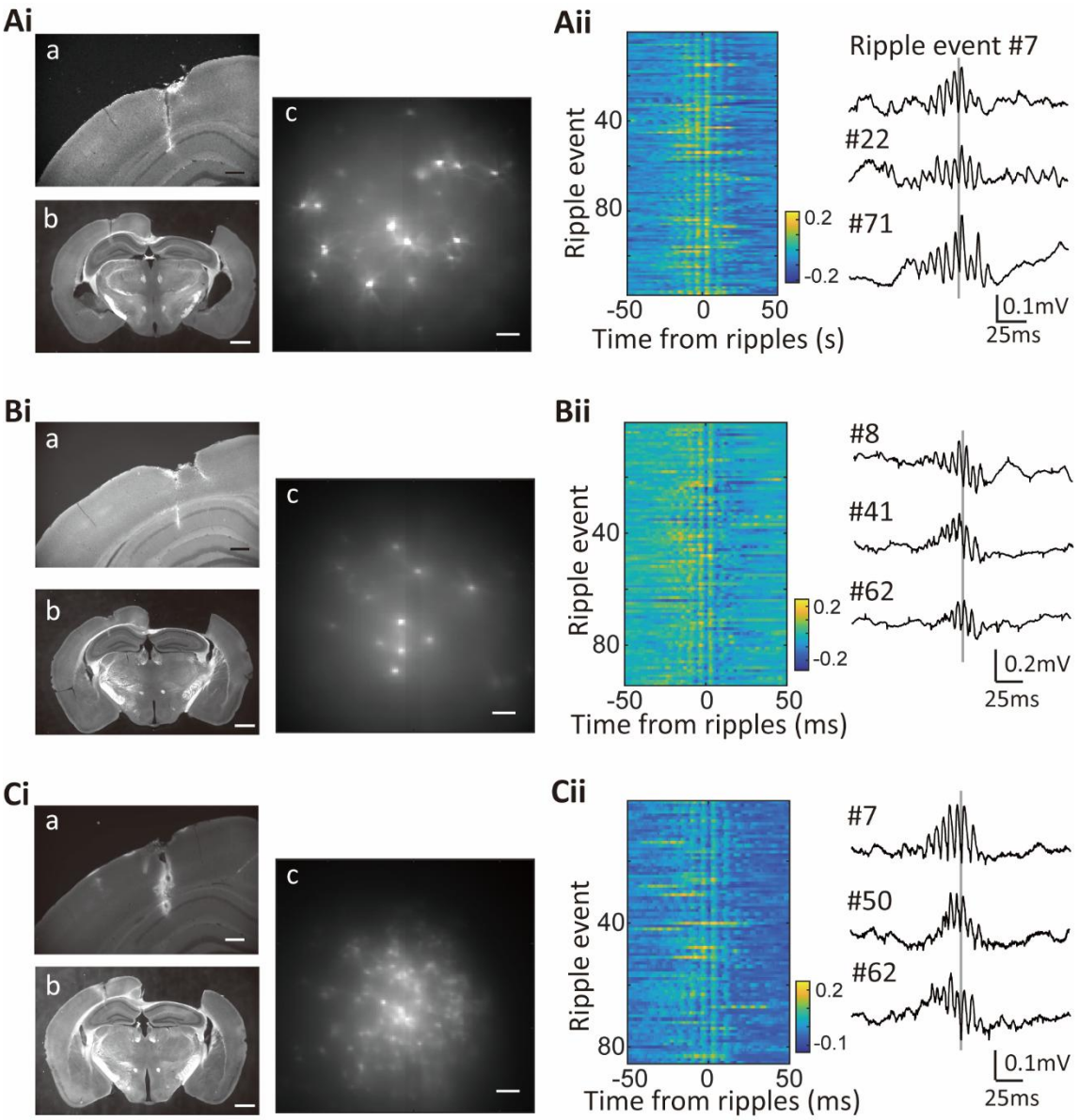

Figure 1-figure supplement 1. Paired photographs of the LFP electrode track and the voltage image from the same animal.

(Ai) Fluorescence images of a brain slice containing the electrode track (a: high magnification; b: low magnification) and the averaged voltage image of CA1 pyramidal cells taken in vivo from the same animal (c). Scale bar: 300 μ m (a), 1 mm (b), and 100 μ m (c).

(Aii) Voltage traces of the LFP recording aligned to the time of maximum ripple power. Left: color-coded voltage traces of all ripple events. Right: representative ripple traces.

(B, C) Same as in (A), but from different animals.

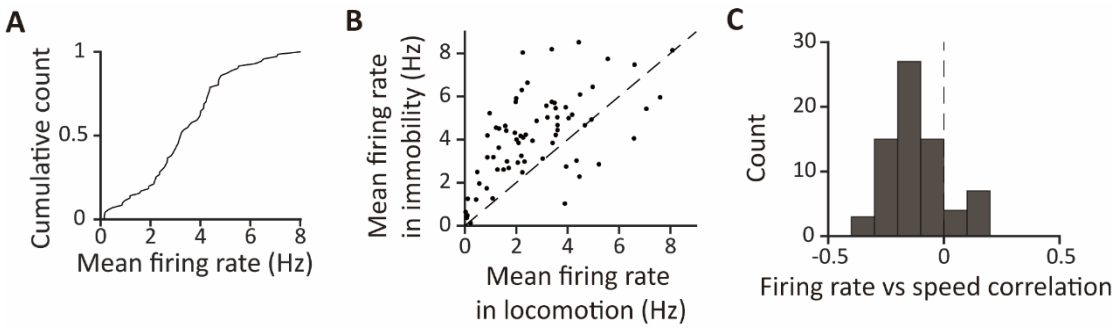

Supplementary Figure 2. Mean firing rate distribution and correlation with animals' speed.

(A) Cumulative distribution of mean firing rates averaged throughout the entire 180-second recording period.

(B) Mean firing rates during locomotion plotted against mean firing rates during immobility for individual cells. Each dot represents a cell. Mean firing rates are higher during immobility than during locomotion (4.2±0.2 Hz for immobility, 2.8±0.2 Hz for locomotion, $t_{(70)}$=6.63, p<0.0001, Student's t-test).

(C) Histogram of correlation coefficients between instantaneous firing rates and the animals' speed for each neuron.

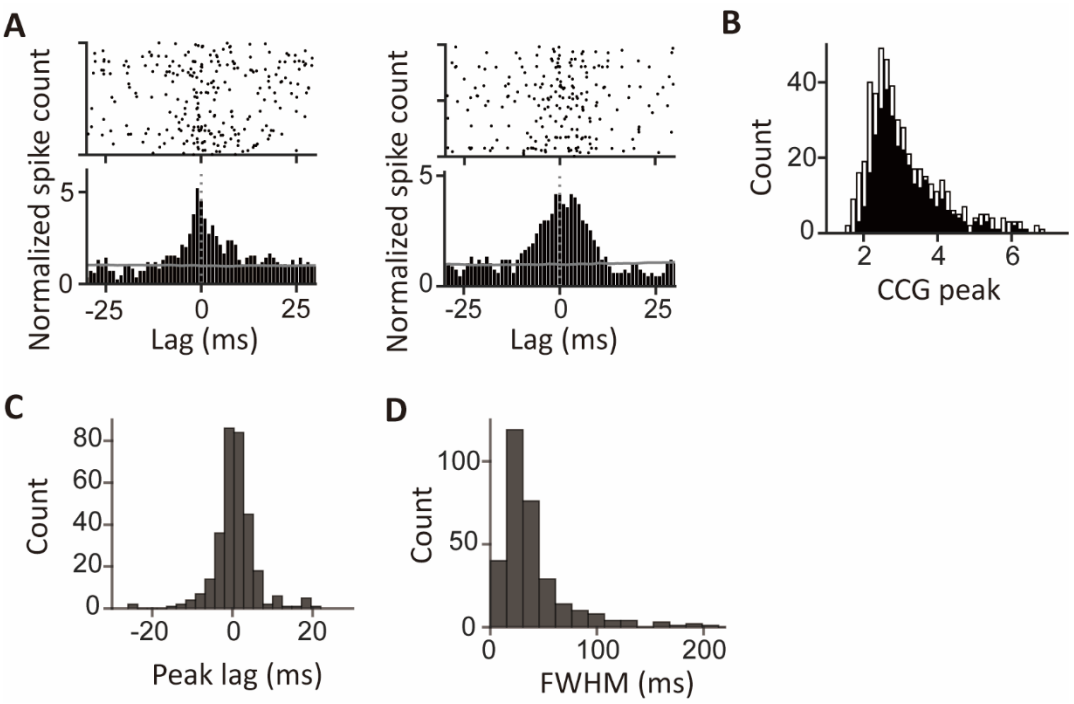

Figure 1-figure supplement 2. Pairwise cross-correlogram (CCG) between CA1 pyramidal cells.

(A) CCGs of two representative cell pairs exhibiting significant peaks compared to the jittered spike trains of the target cells (gray lines).

(B) Distribution of the CCG peaks (*n*=497 pairs). Black: CCG peaks with significance ($p<0.05$). White: CCG peaks without significance ($p>=0.05$).

(C) Histogram of peak lags of significant CCG peaks (*n*=315 pairs).

(D) Histogram of FWHMs of significant CCG peaks (*n*=315 pairs).

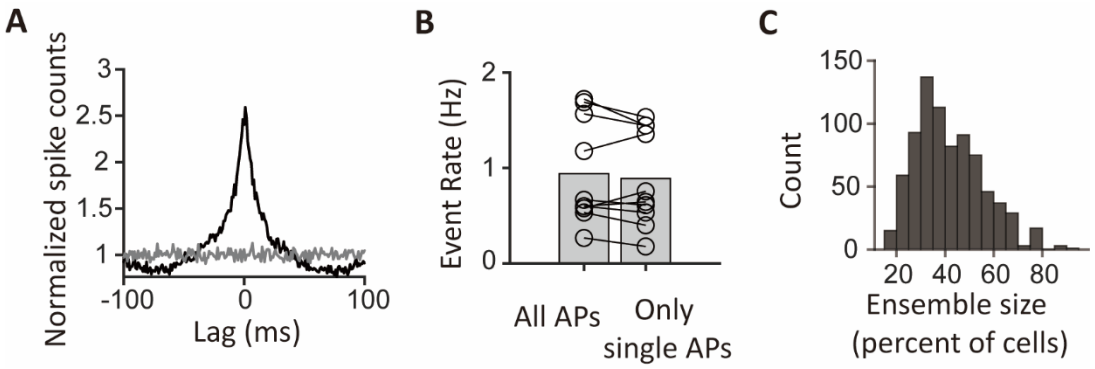

Supplementary Figure 3. Population synchrony remains after removing the later spikes in bursts.

(A) Grand-average cross-correlogram (CCG) calculated using spike trains with the later spikes in bursts removed. The gray line represents the mean grand-average CCG between reference cells and randomly selected cells from different sessions.

(B) Pairwise comparison of population synchrony event rates between spike trains containing all spikes and those with the later spikes in bursts removed. Bar heights represent group means (*n*=10 segments, *p*=0.36, Wilcoxon signed-rank test).

(C) Histogram of ensemble sizes showing the percentage of cells participating in synchronous ensembles.

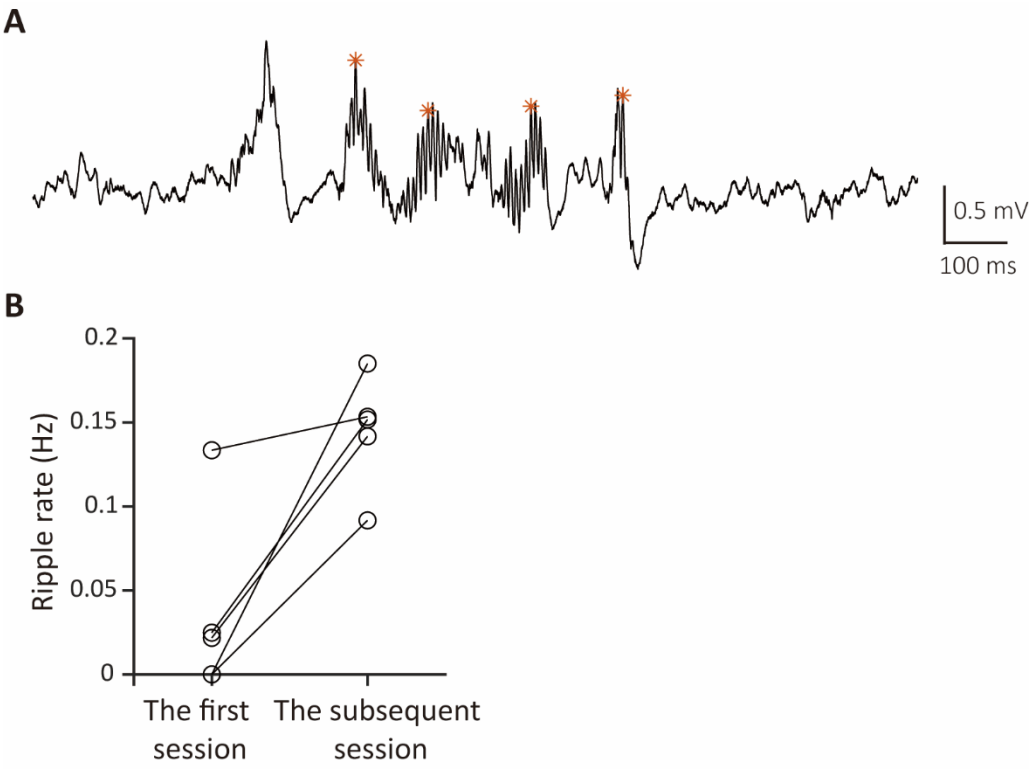

Figure 3-figure supplement 1. LFP ripples recorded in the first and subsequent sessions in a novel maze.

(A) An example LFP trace with ripples recorded in a subsequent session following the first session of novel exploration, where no ripple was detected.

(B) Ripple rates in the first and subsequent sessions recorded in the same animals (n=5 mice) during novel exploration.

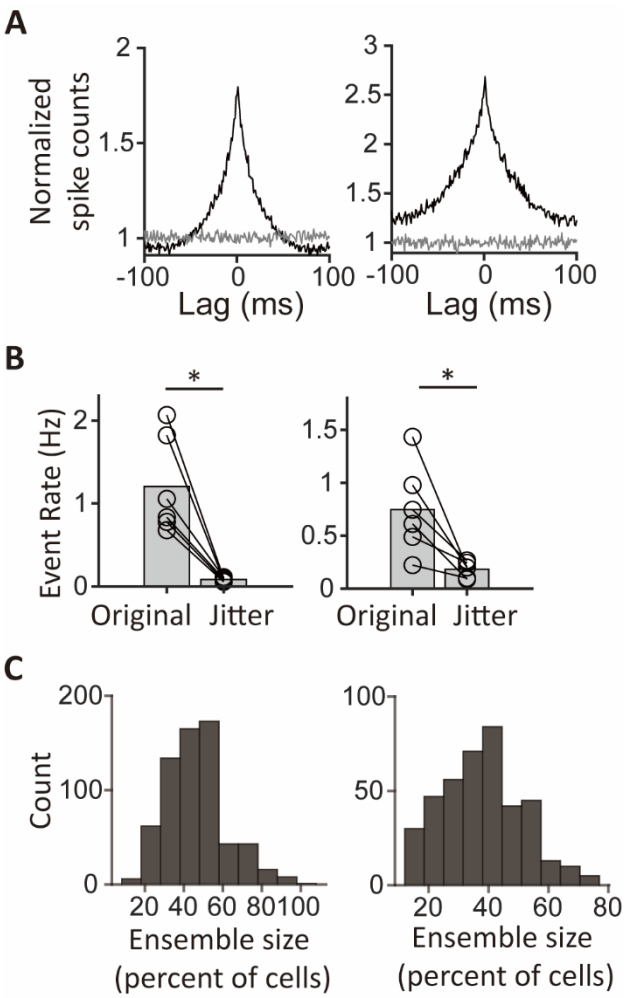

Figure 3-figure supplement 2. Population synchrony during novel immobility.

(A) Grand average cross-correlograms (CCGs) for neurons labeled on E14.5 (left) and on E17.5 (right). The gray line represents the mean grand-average CCG between reference cells and randomly selected cells from different sessions.

(B) Pairwise comparison of synchronous event rates between the original and jittered data. Event rates were significantly higher in the original data compared to jittered controls for E14.5 neurons (left; mean event rate: 1.21 ± 0.24 Hz for the original data, 0.08 ± 0.009 Hz for jittered data, n=6 segments, W=21, p=0.03, Wilcoxon signed-rank test) and E17.5 neurons (right; mean event rate: 0.75 ± 0.17 Hz for the original data, 0.18 ± 0.03 Hz for jittered data, n=6 segments, W=21, p=0.03, Wilcoxon signed-rank test). Bar heights represent group means. *p<0.05

(C) Histograms of ensemble sizes showing the percentage of cells participating in synchronous ensembles for E14.5 neurons (left) and E17.5 neurons (right).

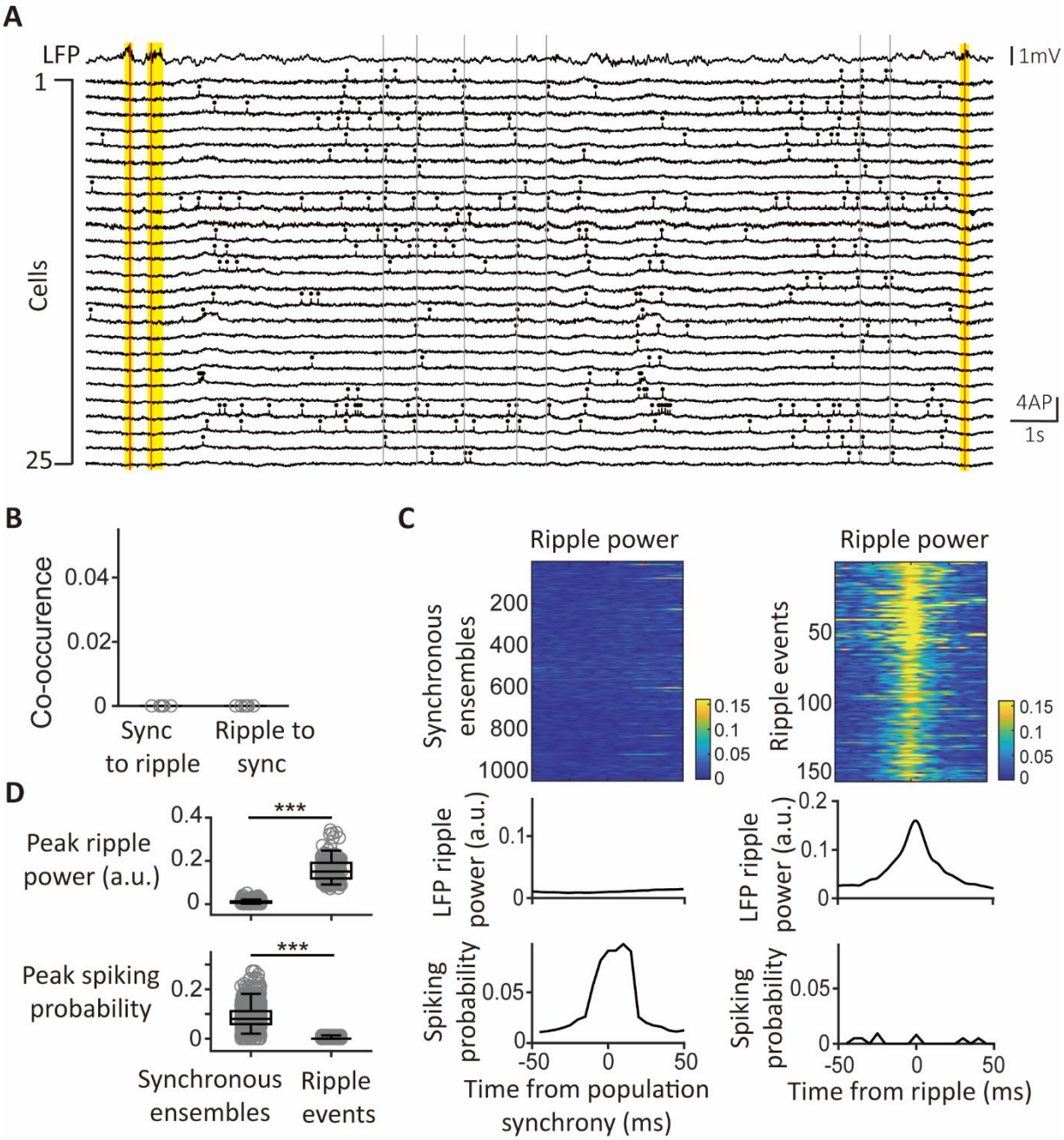

Figure 3-figure supplement 3. Population synchrony outside ripple episodes during novel immobility.

(A) Example traces illustrating the distinct timings of ripple episodes and synchronous ensembles. Top: Simultaneously recorded LFP trace showing episodes of ripple oscillations. Red vertical lines indicate the timings of peak ripple power in the LFP trace, while yellow vertical bars mark the duration of ripple episodes. Bottom: Fluorescence traces from 25 CA1PCs. Gray vertical lines indicate the timings of synchronous ensembles.

(B) Percentages of co-occurrence between synchronous ensembles and ripple events. The “sync to ripples” group represents the percentage of ripple events that co-occur with synchronous ensembles, while the “ripples to sync” group shows the percentage of synchronous ensembles that co-occur with ripple events. Each gray circle represents an individual session.

(C) LFP ripple power and spiking probability aligned to synchronous ensembles and ripple events. **Upper panel**: Color-coded LFP power at ripple frequency (120-240Hz), aligned to the timings of 1052 synchronous ensembles (left) and 174 ripple events (right). **Middle panel**: Average LFP power at ripple frequencies aligned to the timings of synchronous ensembles (left) and ripple events (right). **Lower panel**: Average spiking probability of all recorded cells aligned to the timings of synchronous ensembles (left) and ripple events (right).

(D) Boxplots and comparisons of peak ripple power (upper panel) and peak spiking probability (lower panel) at the timings (t=0) of population synchrony (left) and ripple events (right). For peak ripple power: $p<0.001$, $t_{(1224)}=86.6$, Student’s *t*-test; for peak spiking probability: $p<0.001$, $t_{(1224)}=24.3$, Student’s *t*-test. Gray circles indicate peak values for individual triggered traces.

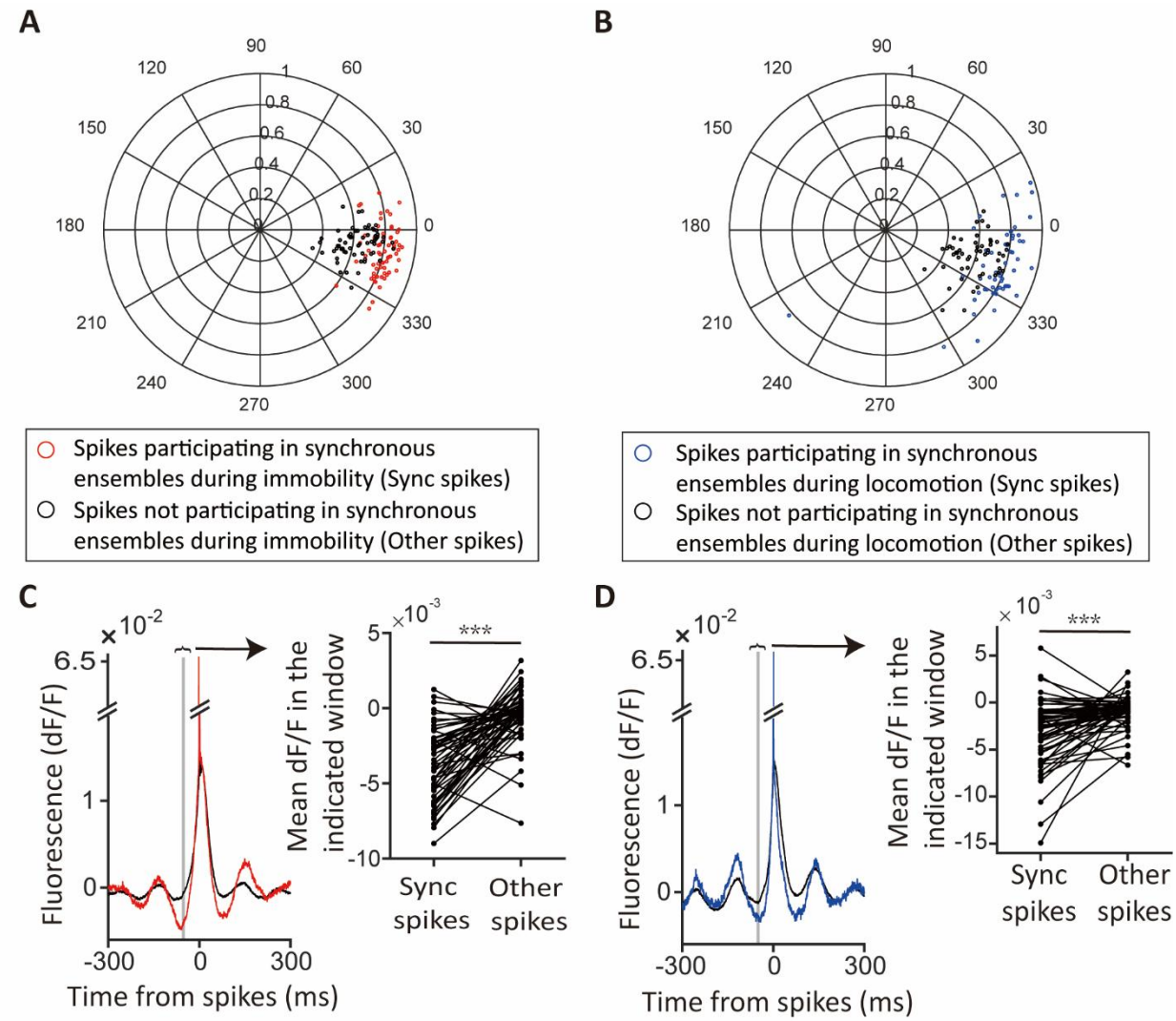

Figure 5-figure supplement 1. SubVm theta modulation of spikes during immobility and locomotion periods of novel exploration.

(A) Polar plot comparing subVm theta modulation between spikes participating in synchronous ensembles (sync spikes) and spikes not participating in synchronous ensembles (other spikes) during immobility. Each dot represents the averaged modulation of a cell. Cells with modulation strengths that are not significant are excluded in the plot and in the comparison. The modulation strengths of spikes participating in synchrony are significantly higher than those of spikes not participating in synchrony (modulation strength for spikes participating in synchronous ensembles: 0.81±0.07, for spikes not participating in synchronous ensembles: 0.64±0.11, mean±s.d., $t_{(64)}$=12.6, p<0.001, paired t-test).

1278 **(B)** Same as in (A), but during locomotion (modulation strength for spikes participating in
1279 synchronous ensembles: 0.80±0.09, for spikes not participating in synchronous ensembles: 0.60±
1280 0.12, mean±s.d., $t_{(53)}$=12.3, p<0.001, paired t-test).
1281 **(C)** Average fluorescence triggered by cells' spikes participating in synchronous ensembles (red, sync
1282 spikes) and not participating in synchronous ensembles during immobility (black, other spikes; n=59
1283 cells). Inset: Pairwise comparison of average fluorescence 50±5 ms before time of spikes (t=0)
1284 between the two triggered groups (n=59 cells, p<0.001, paired t-test). ***p<0.001.
1285 **(D)** Same as in (C), but during locomotion. Inset: Pairwise comparison of average fluorescence (n=59
1286 cells, p<0.001, paired t-test).
1287

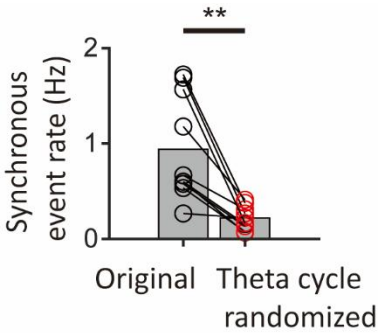

Supplementary Figure 4. Significant reduction of population synchrony by randomizing spikes across theta cycles while preserving phases

Pairwise comparison of population synchrony event rates between the original spike trains and randomized spike trains, in which spike timings were shuffled across theta cycles while preserving phases (*n*=10 segments, *p*=0.002, Wilcoxon signed-rank test). Bar heights represent group means.

** *p*<0.01

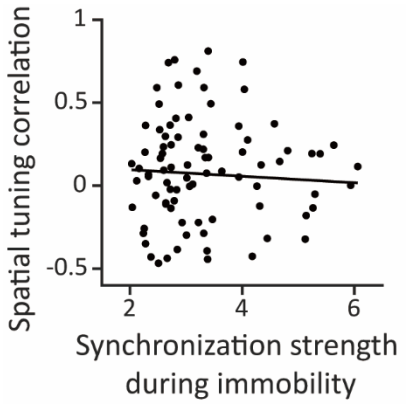

Figure 5-figure supplement 1. Synchronization strengths during immobility show little correlation with the similarity of spatial tunings between place cells. Synchronization strengths during immobility plotted against correlation coefficients of spatial tunings for pairs of place cells. Synchronization strengths show little correlation with similarities of spatial tunings (Spearman correlation coefficient=-0.003, *p*=0.98, *n*=88 cell pairs).

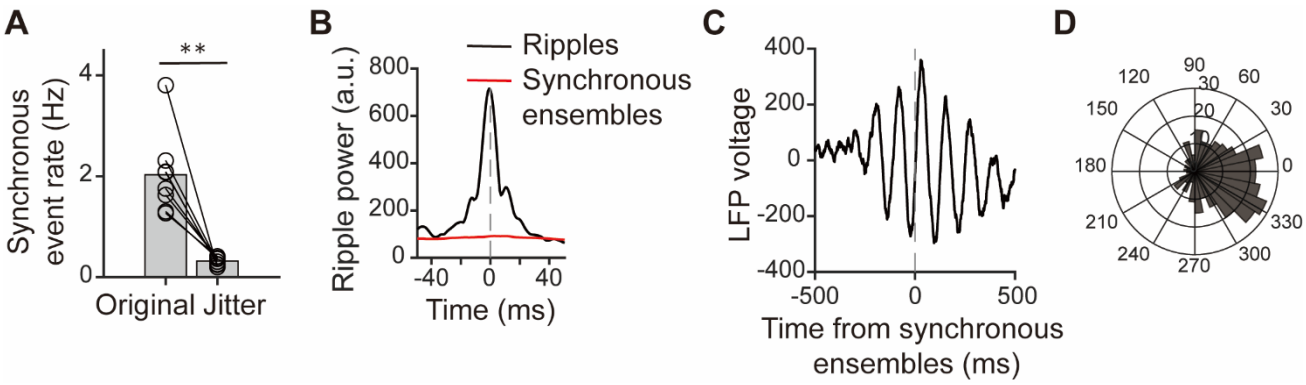

Supplementary Figure 5. Analyses of synchronous ensembles in the publicly available data

(A) Pairwise comparison of synchronous event rates between the original and jittered data. Event rates were significantly higher in the original data compared to jittered controls (n=8 sessions, p=0.008, Wilcoxon signed-rank test). Bar heights represent group means. **p<0.01.

(B) Dynamics of ripple power aligned to timings of ripples (black) and timings of synchronous ensembles (red).

(C) Average LFP trace aligned to timings of synchronous ensembles of a session.

(D) Polar histogram of the differences between theta phases of individual synchronous ensembles and the preferred phase of the session.